Article

Cell Reports

p63 and SOX2 Dictate Glucose Reliance and Metabolic Vulnerabilities in Squamous Cell Carcinomas

Graphical Abstract

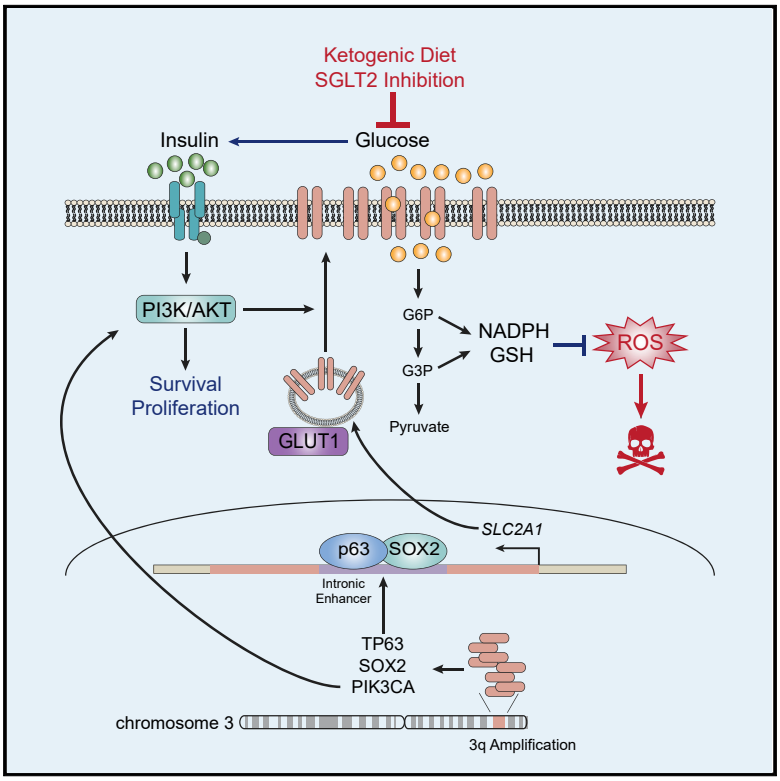

Authors

Meng-Hsiung Hsieh, Joshua H. Choe, Jashkaran Gadhvi, ..., Ralph J. DeBerardinis, Tae Hoon Kim, Jung-whan Kim

Correspondence

jay.kim@utdallas.edu

In Brief

Hsieh et al. show that p63 and SOX2 cooperate to induce enhanced GLUT1 expression, driving a critical reliance on glucose, in squamous cell carcinomas. Systemic glucose restriction by ketogenic diet or SGLT2 inhibition attenuates squamous tumor progression by disrupting redox homeostasis and insulin/AKT pathways *in vivo*.

Highlights

- p63 and SOX2 drive elevated GLUT1 expression by *SLC2A1* intronic enhancer transactivation
- Enhanced GLUT1-mediated glucose influx fuels antioxidant production to promote survival
- Systemic glucose restriction concurrently targets vital metabolic and oncogenic pathways
- High random blood glucose is associated with poorer outcomes in squamous cancer patients

Hsieh et al., 2019, Cell Reports *28*, 1860–1878
August 13, 2019
https://doi.org/10.1016/j.celrep.2019.07.027

CellPress

OPEN ACCESS
CellPress

Cell Reports
Article

p63 and SOX2 Dictate Glucose Reliance and Metabolic Vulnerabilities in Squamous Cell Carcinomas

Meng-Hsiung Hsieh,[1] Joshua H. Choe,[2] Jashkaran Gadhvi,[1] Yoon Jung Kim,[1] Marcus A. Arguez,[1] Madison Palmer,[1] Haleigh Gerold,[1] Chance Nowak,[1] Hung Do,[1] Simbarashe Mazambani,[1] Jordan K. Knighton,[1] Matthew Cha,[1] Justin Goodwin,[4] Min Kyu Kang,[5] Ji Yun Jeong,[6] Shin Yup Lee,[7] Brandon Faubert,[8] Zhenyu Xuan,[1,9] E. Dale Abel,[10] Claudio Scafoglio,[11] David B. Shackelford,[11] John D. Minna,[12] Pankaj K. Singh,[13] Vladimir Shulaev,[14] Leonidas Bleris,[3] Kenneth Hoyt,[3] James Kim,[15] Masahiro Inoue,[16] Ralph J. DeBerardinis,[8,17] Tae Hoon Kim,[1] and Jung-whan Kim[1,18,*]

[1]Department of Biological Sciences, The University of Texas at Dallas, Richardson, TX, USA
[2]Department of Biological Sciences, Columbia University, New York, NY, USA
[3]Department of Bioengineering, The University of Texas at Dallas, Richardson, TX, USA
[4]Graduate School of Art and Sciences and School of Medicine, Yale University, New Haven, CT, USA
[5]Department of Radiation Oncology, School of Medicine, Kyungpook National University, Daegu, Korea
[6]Department of Pathology, School of Medicine, Kyungpook National University, Daegu, Korea
[7]Department of Internal Medicine, School of Medicine, Kyungpook National University, Daegu, Korea
[8]Children's Medical Center Research Institute, University of Texas Southwestern Medical Center, Dallas, TX, USA
[9]Center for Systems Biology, The University of Texas at Dallas, Richardson, TX, USA
[10]Division of Endocrinology and Metabolism and the Fraternal Order of Eagles Diabetes Research Center, Roy J. and Lucille A. Carver College of Medicine, University of Iowa, Iowa City, IA, USA
[11]Department of Pulmonary and Critical Care Medicine, David Geffen School of Medicine, University of California, Los Angeles, CA, USA
[12]Hamon Center for Therapeutic Oncology Research, Simmons Comprehensive Cancer Center, Departments of Medicine and Pharmacology, University of Texas Southwestern Medical Center, Dallas, TX, USA
[13]Eppley Institute for Cancer Research, University of Nebraska Medical Center, Omaha, NE, USA
[14]Department of Biological Sciences, College of Science, Advanced Environmental Research Institute, University of North Texas, Denton, TX, USA
[15]Department of Internal Medicine, Hamon Center for Therapeutic Oncology Research, and Simmons Comprehensive Cancer Center, University of Texas Southwestern Medical Center, Dallas, TX, USA
[16]Department of Clinical Bio-resource Research and Development, Graduate School of Medicine, Kyoto University, Kyoto, Japan
[17]Howard Hughes Medical Institute, University of Texas Southwestern Medical Center, Dallas, TX, USA
[18]Lead Author
*Correspondence: jay.kim@utdallas.edu
https://doi.org/10.1016/j.celrep.2019.07.027

SUMMARY

Squamous cell carcinoma (SCC), a malignancy arising across multiple anatomical sites, is responsible for significant cancer mortality due to insufficient therapeutic options. Here, we identify exceptional glucose reliance among SCCs dictated by hyperactive GLUT1-mediated glucose influx. Mechanistically, squamous lineage transcription factors p63 and SOX2 transactivate the intronic enhancer cluster of *SLC2A1*. Elevated glucose influx fuels generation of NADPH and GSH, thereby heightening the anti-oxidative capacity in SCC tumors. Systemic glucose restriction by ketogenic diet and inhibiting renal glucose reabsorption with SGLT2 inhibitor precipitate intratumoral oxidative stress and tumor growth inhibition. Furthermore, reduction of blood glucose lowers blood insulin levels, which suppresses PI3K/AKT signaling in SCC cells. Clinically, we demonstrate a robust correlation between blood glucose concentration and worse survival among SCC patients. Collectively, this study identifies the exceptional glucose reliance of SCC and suggests its candidacy as a highly vulnerable cancer type to be targeted by systemic glucose restriction.

INTRODUCTION

Squamous cell carcinoma (SCC) is a major class of malignancy arising from squamous cells of the epithelia and is responsible for more than one million cancer deaths annually worldwide (Dotto and Rustgi, 2016; Yan et al., 2011). Despite the trend toward molecularly targeted therapy for certain cancers, SCC patients have benefited very little from the application of such therapeutic options due to a lack of identified vulnerabilities. Rather, decades old platinum-based chemotherapy or radiation regimens still remain the first-line treatment options and, thus, retain limited specificity to the unique characteristics of SCC (Dotto and Rustgi, 2016). SCCs originate from stratified epithelial layers of various anatomical sites (Yan et al., 2011). Despite the unique microenvironmental cues of the tissues where SCCs arise, the majority of SCCs share common oncogenic abnormalities, such as the amplification of chromosome

3q, which contains important transcriptional regulators p63 and SOX2 (Cancer Genome Atlas, 2015; Cancer Genome Atlas Research Network, 2012; Cancer Genome Atlas Research Network et al., 2017a; Cancer Genome Atlas Research Network et al., 2017b).

p63, part of the p53 protein family, is a master transcription factor of stem cell pluripotency and remains crucial in basal epithelial development, differentiation, and prevention of senescence (Crum and McKeon, 2010; Su et al., 2013). Recent studies have established the oncogenicity of amplified ΔNp63, an isoform that lacks the N-terminal transactivation (TA) domains as a result of an alternative transcriptional start site, in squamous cancer development and progression. Amplified ΔNp63 may cooperate with various oncogenic events, including activation of oncogenic Ras and β-catenin as well as repression of tumor suppressors p53 and p73, to endow an increased proliferative effect (Hibi et al., 2000; Keyes et al., 2011; Patturajan et al., 2002; Rocco et al., 2006; Yang et al., 1998). Analogous to ΔNp63, SOX2, a key transcriptional regulator that is crucial for embryonic stem cell pluripotency maintenance and cell fate determination (Gubbay et al., 1990; Sinclair et al., 1990), is frequently amplified and drives oncogenic growth in various SCCs (Bass et al., 2009). Ectopic SOX2 expression in autochthonous mouse models of lung cancer resulted in squamous lineage restriction (Ferone et al., 2016). Intriguingly, p63 and SOX2 have been reported to jointly occupy multiple genomic loci in esophageal and lung SCC cell lines (Watanabe et al., 2014). Collectively, these studies indicate that p63 and SOX2 may cooperate to generate a squamous lineage-specific transcriptional program that promotes the oncogenic progression of SCC and the reliance on which may present a targetable vulnerability. Here, we seek to further uncover the precise mechanism through which p63 and SOX2 cooperatively exert a SCC-specific oncogenic phenotype.

In addition to oncogene reliance, a deregulated metabolism, in order to support the unique bioenergetic as well as anabolic needs of rapidly proliferating cells, represents another defining malignant abnormality of cancer (Vander Heiden and DeBerardinis, 2017). Constitutively augmented glycolysis even in the presence of adequate oxygen, known as the Warburg effect (Warburg, 1956a, 1956b), is thought to support cancer progression by helping cancer cells meet their enhanced needs for energy, macromolecular biosynthesis, and redox homeostasis. Although these pivotal functions of glycolysis were considered a universal feature of cancer metabolism, an increasing body of evidence argues for substantial heterogeneity in glucose metabolism among diverse cancer types and regional metabolic heterogeneity even within the same tumor (Gentric et al., 2017; Hensley et al., 2016). For example, our recent study demonstrated a distinct metabolic heterogeneity between two subtype tumors of non-small-cell lung cancer (NSCLC), lung squamous cell carcinoma (LSCC), and lung adenocarcinoma (LADC) (Goodwin et al., 2017). LSCC exhibits distinctively elevated glucose transporter 1 (GLUT1) expression resulting in a high reliance on glucose, whereas LADC is significantly less dependent on glucose for survival and tumor growth.

In light of this distinct metabolic heterogeneity, we sought to expand our analysis to other major SCC and non-SCC tumors. Our results reveal that hyper-activation of GLUT1-mediated glycolytic influx is phenotypically embedded in all major SCCs and not only LSCC, suggesting a previously unrecognized unifying metabolic signature among SCCs. Here, our study uncovers that GLUT1 is a direct transcriptional target of p63 and SOX2, by which the p63 and SOX2 complex binds to and transactivates the intronic enhancer cluster of the *SLC2A1* gene that encodes GLUT1, resulting in markedly elevated GLUT1 expression. GLUT1-mediated glucose influx fuels generation of nicotinamide adenine dinucleotide phosphate (NADPH) from the pentose phosphate pathway (PPP), which provides a sustaining anti-oxidative capacity that is required for the survival and tumor growth of SCCs. Moreover, glucose restriction by ketogenic diet, inhibition of renal glucose reabsorption with US Food and Drug Administration (FDA)-approved SGLT2 inhibitor canagliflozin, and genetic ablation of the *SLC2A1* gene effectively and specifically suppressed the tumor growth of SCC xenografts as well as autochthonous transgenic mouse models. Together, these results not only provide mechanistic insight into squamous lineage-specific metabolic regulation through an enhancer region of *SLC2A1* but also define metabolic vulnerabilities imposed by the exquisite glucose reliance of SCC. This study further presents a viable treatment paradigm in targeting squamous cancers metabolically by modulating organismal level blood glucose levels and canonical insulin/phosphatidylinositol 3-kinase (PI3K)/AKT signaling by dietary as well as pharmacological glucose restriction.

RESULTS

Robust GLUT1 Expression Defines a Unifying Metabolic Feature of SCCs

We recently reported that GLUT1 is distinctively overexpressed in the SCC subtype of NSCLC, resulting in a strict reliance on glucose and a high susceptibility to glycolytic inhibition (Goodwin et al., 2017). However, SCC arises from multiple anatomical sites in addition to the lung (Yan et al., 2011). Thus, we sought to determine if GLUT1 overexpression is phenotypically associated with squamous lineage malignancy. The Cancer Genome Atlas (TCGA) analysis of mRNA sequencing gene expression profiles revealed that all four annotated head and neck (HN), lung, esophageal, and cervical SCCs are the highest GLUT1-expressing cancers (Figure 1A). Notably, a significant proportion of the bladder urothelial carcinoma (BLCA) cohort, which is the fifth-highest GLUT1-expressing tumor type, exhibits a squamous gene expression pattern, yet, squamous patients have not been annotated (Cancer Genome Atlas Research Network, 2014). Analysis of other glucose transporters validates that GLUT1 is the predominant glucose transporter in SCCs (Figure S1A). Experimentally validating TCGA results, immunohistochemical (IHC) analysis of human SCC tissue microarrays demonstrates that GLUT1 is remarkably and specifically overexpressed in all SCCs tested as compared to non-squamous subtypes (Figures 1B and S1B). Moreover, we observed exclusive GLUT1 overexpression in squamous tumor areas within lung and cervical mixed adenosquamous carcinoma tumor tissues (Li and Lu, 2018) (Figures 1C and S1C). GLUT1 mRNA and

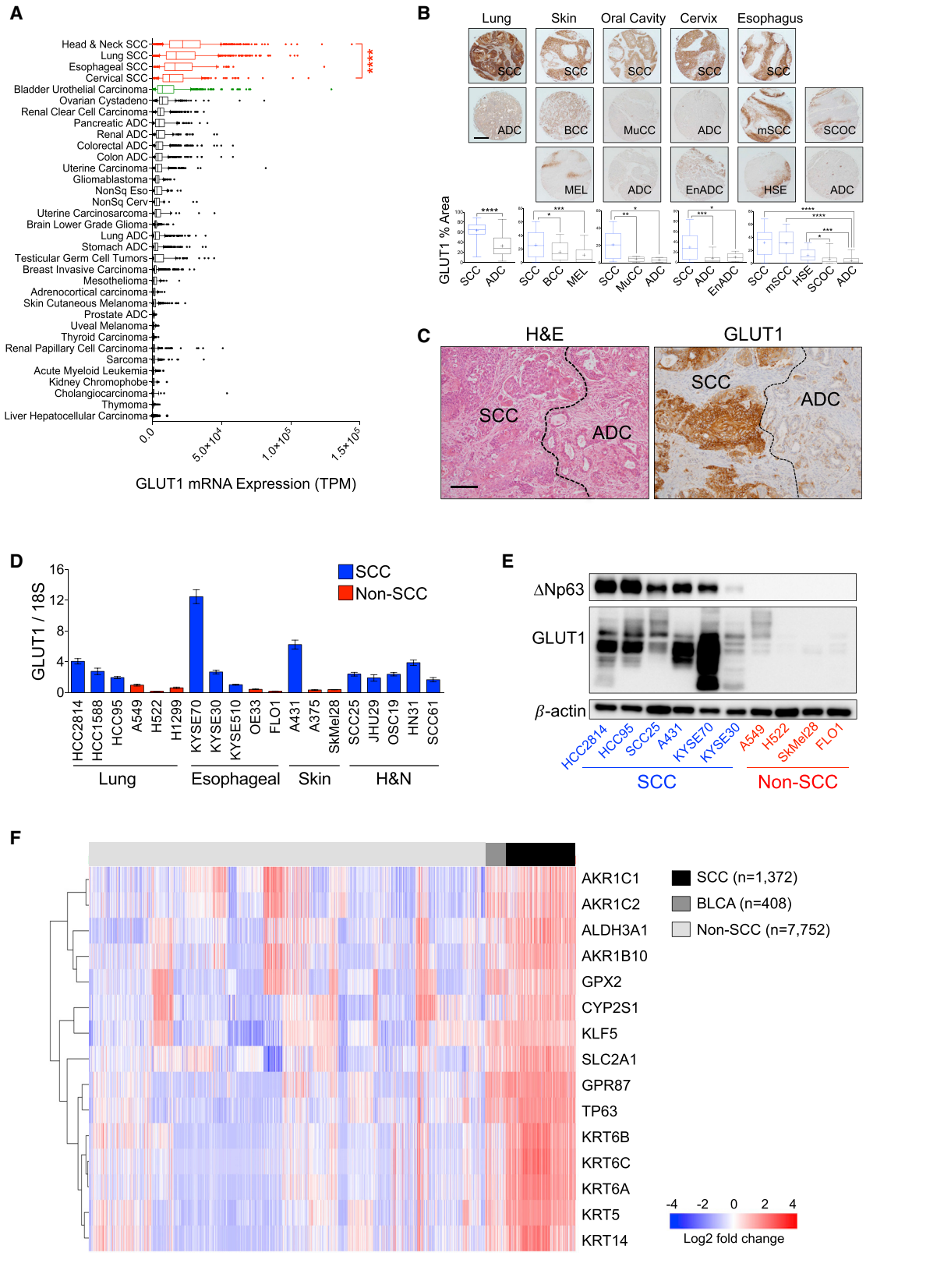

(legend on next page)

protein expression is also highly elevated in a panel of SCC cell lines as compared to non-SCC cell lines (Figures 1D and 1E). GLUT1 expression levels are strongly correlated with the expression of SCC-specific markers, ΔNp63, cytokeratin 5 (CK5, *KRT5*), and cytokeratin 6A (CK6A, *KRT6A*) (Figures 1E and S1D). Next, we performed a differential gene expression analysis by comparing the combined TCGA cohort of all four SCCs (n = 1,372) to all non-SCC tumors (n = 7,752). The analysis identified GLUT1 (*SLC2A1*) among the most significantly upregulated genes in the combined SCC cohort, along with genes associated with squamous differentiation and carcinogenesis (*TP63*, *KRTs*, *GPR87*, and *KLF5*) and oxidative detoxification (*AKRs*, *ALDH3A1*, *GPX2*, and *CYP2S1*) (Dotto and Rustgi, 2016) (Figures 1F and S2A). The BLCA cohort (n = 408) was analyzed as a separate group due to the lack of subtype annotation but exhibited a correspondingly SCC-like expression pattern (Cancer Genome Atlas Research Network, 2014). Collectively, these results uncovered remarkably heightened GLUT1 upregulation as a potent and unique metabolic characteristic embedded in squamous lineage cancers.

p63 Regulates GLUT1 Expression

We next sought to identify the mechanisms underlying universal GLUT1 upregulation in SCCs. Previous studies and our TCGA copy number variation (CNV) analysis have shown that transcription factor p63 is highly expressed in major SCCs mainly through genomic amplification of chromosome 3q26 and functions as a squamous lineage-specific oncogene (Figure S3A) (Hibi et al., 2000; Ramsey et al., 2013). Moreover, we identified a robust correlation between GLUT1 and p63 mRNA expression in individual as well as combined SCC TCGA cohorts (Figures S3B and S3C). We validated the p63/GLUT1 correlation in human SCC tumor tissues by co-immunofluorescent (IF) staining for p63 and GLUT1 (Figure 2A). To assess the potential link between p63 and GLUT1, we performed short hairpin RNA (shRNA)-mediated knockdown of p63 in lung (HCC95 and HCC2814), esophageal (KYSE70), and HN (JHU-029) SCC cell lines and observed that p63 knockdown remarkably decreased GLUT1 mRNA and protein expression (Figures 2B and S3D). Immunocytochemistry (ICC) staining confirmed the attenuation of GLUT1 levels at the plasma membrane in p63 knockdown SCC cell lines (Figures 2C and S3E).

The p63 gene (TP63) expresses two major isoforms, TAp63 and amino terminally truncated ΔNp63 (Crum and McKeon, 2010; Su et al., 2013). As ΔNp63 is generally the predominant isoform expressed in squamous cancer cells (Rocco and Ellisen, 2006), we validated that ΔNp63 is indeed predominantly expressed in a panel of SCC cell lines (Figure S4A), whereas TAp63 was undetectable by immunoblot assays. To confirm that ΔNp63 is responsible for GLUT1 expression, we employed isoform-specific shRNAs to knock down ΔNp63 or TAp63. ΔNp63-specific knockdown consistently suppressed GLUT1 mRNA and protein expression in SCC cell lines (Figure 2D), whereas TAp63 knockdown showed no effect on GLUT1 expression or glucose uptake (Figures S4B and S4C). Conversely, we ectopically introduced ΔNp63 or TAp63 and observed that only ectopically expressed ΔNp63 further increased GLUT1 mRNA, protein levels, and glucose uptake in SCC cell lines (Figures 2E, 2F, S4D, and S4E). These results indicate that ΔNp63 but not TAp63 isoforms transcriptionally activate GLUT1 expression in SCCs.

We next investigated whether GLUT1 is a direct target of p63. Global DNA binding of p63 across the genome has been well characterized (Bao et al., 2015; Kouwenhoven et al., 2015). Analysis of the publically available dataset of the HN SCC cell line JHU-029 identified strong p63 chromatin immunoprecipitation sequencing (ChIP-seq) signal clusters within the second intron of the GLUT1 gene (*SLC2A1*) (Saladi et al., 2017) (Figure 2G). Intriguingly, an epigenetic mark of potential enhancer elements, H3K27ac, is co-localized with p63 binding regions (Kundaje et al., 2015; Zhang et al., 2016) (Figure 2G). Corroborating the ChIP-seq dataset, our ChIP assays identified strong p63 and H3K27ac binding signals in all three individual potential enhancer elements (E1–E3) on the second intronic region of *SLC2A1* but not on the first intronic region of *SLC2A1* or the gene desert region (NC, negative control) (Figures 2H). Furthermore, we observed a significant induction of luciferase expression in the potential enhancer-containing reporter construct, whereas ΔNp63 knockdown reduced luciferase reporter activity, thus validating the specificity of p63-mediated transcriptional activation of GLUT1 (Figures 2D and 2I). To further validate p63 binding to the potential *SLC2A1* enhancer in physiologically relevant conditions, we disrupted the p63-binding site in E2 by CRISPR-Cas9-mediated genome editing. Notably, GLUT1 expression was significantly reduced in edited clones containing the deletion (Figure 2J). Collectively, these data suggest that p63-dependent transactivation of *SLC2A1* enhancer clusters is the mechanistic basis for GLUT1 overexpression across all SCCs.

Figure 1. Enhanced GLUT1 Expression and Glycolytic Metabolism in SCC

(A) RNA sequencing (RNA-seq) analysis of GLUT1 mRNA expression among 35 tumor types. Each box represents the lower quartile, median, and upper quartile. Whiskers represent the 10th and 90th percentile of the data. Kruskal-Wallis nonparametric ANOVA. TPM, transcripts per million.

(B) Representative IHC images (top) and quantification (bottom) of GLUT1 expression in human lung (n = 237), skin (n = 50), oral cavity (n = 43), cervix (n = 198), and esophagus (n = 54) SCC and non-SCC tumor tissue microarray (top). Scale bars, 1 mm. Each box represents the lower quartile, median, and upper quartile. Whiskers represent the 10th and 90th percentile of the data. Mann-Whitney *U*-test or one-way ANOVA. BCC, basal cell carcinoma; MEL, melanoma; MuCC, mucoepidermoid carcinoma of salivary gland; EnADC, endometrioid ADC; mSCC, metastatic SCC, HSE, hyperplasia of squamous epithelium; SCOC, small cell esophageal carcinoma.

(C) H&E staining and IHC images of GLUT1 expression in human lung adenosquamous carcinoma tumor samples. Scale bar, 300 μm.

(D) qRT-PCR analysis of GLUT1 mRNA expression in SCC and non-SCC cell lines (n = 3 for each cell line).

(E) Immunoblot analysis of ΔNp63 and GLUT1 expression in SCC and non-SCC cell lines.

(F) Representative heatmap depicting differential gene expression between the combined TCGA cohorts of NH, lung, cervical, and esophageal SCC (n = 1,372), bladder urothelial carcinoma (BLCA; n = 408), and all non-SCC (n = 7,752) tumors. Extended gene heatmap with clustering information is provided in Figure S2A.

All error bars represent the mean ± SEM. ****p < 0.0001, ***p < 0.001, **p < 0.01, *p < 0.05. Two-tailed t test was used unless noted otherwise.

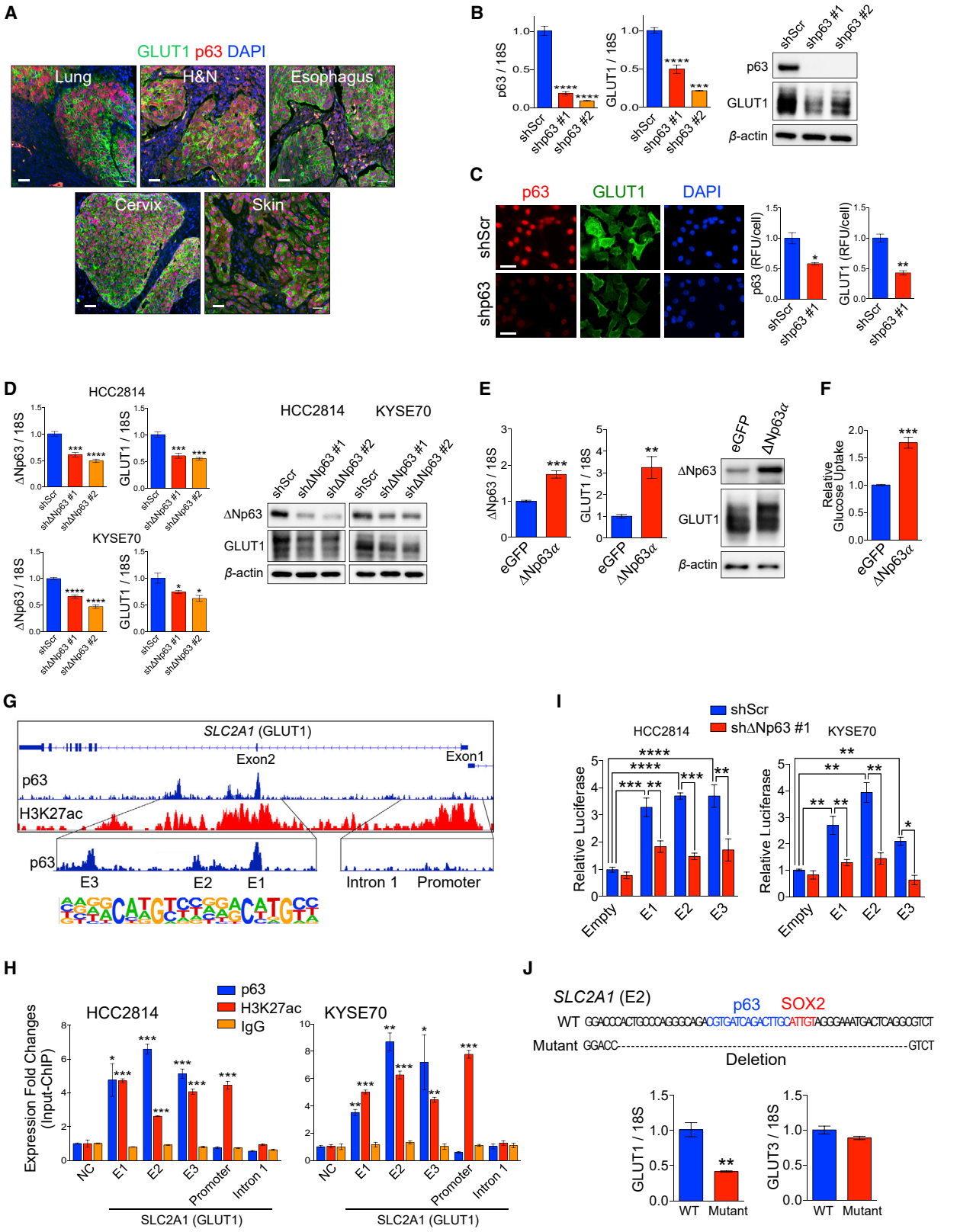

(legend on next page)

p63/GLUT1-Mediated Glucose Influx Provides Anti-oxidative Capacity in SCCs

Cancer cells can exploit enhanced glucose influx to promote cellular proliferation and survival. The glucose-fueled generation of NADPH from the oxidative PPP and glutathione (GSH) by *de novo* serine biosynthesis provides sustaining anti-oxidative capacity in cancer cells (Figure 3A) (Locasale and Cantley, 2011). Metabolic tracing analysis using [U-^{13}C] glucose indicates that SCC cells exhibit significantly higher glucose consumption and synthesis of ribose-5-phosphate (R5-P) and serine from glucose as compared to non-SCC cells (Figures 3B, S5A, and S5B). These data suggest that p63/GLUT1-mediated increased glucose influx fuels anabolic pathways to generate NADPH and GSH in SCC. This enhanced redox potential renders SCC cells more resistant to high concentrations of vitamin C and buthionine sulfoximine (BSO), which have been shown to act as pro-oxidants by depleting cellular GSH (Yun et al., 2015) (Figures 3D and S6A). Accordingly, SCC cells produced considerably less reactive oxygen species (ROS) than non-SCC cells in response to vitamin C (1 mM) treatment (Figure 3E), suggesting augmented anti-oxidative capacities in SCCs.

We next sought to investigate whether p63/GLUT1-mediated glucose influx maintains cellular redox homeostasis in SCC. p63 knockdown markedly suppressed glucose influx into R5-P, serine, and lactate in SCC cells (Figures 3C, S5C, S6B, and S6C). Accordingly, reduced glucose influx into anabolic pathways by p63 or GLUT1 knockdown resulted in increases in cellular ROS measured by a universal oxidative indicator, 2′-7′-dichlorodihydrofluorescein (H_2DCFDA) (Figure 3F), a small molecule probe for superoxide radicals, dihydroethidium (DHE) (Figure 3G), and a lipid peroxidation sensor, C11-BODIPY (Figure S6D). Importantly, increased ROS upon p63 or GLUT1 knockdown is associated with significant reduction in intracellular NADPH/NADP+ and GSH/GSSG ratios (Figures 3H, 3I, and S6E), *in vitro* cell proliferation (Figures 3J and S6F), and transformation capacity (Figure 3K). Restoring cellular oxidative capacity by supplementing with an anti-oxidant, N-acetylcysteine (NAC), markedly rescued the cellular proliferation and viability of p63-deficient SCC cells, thereby implicating elevated ROS upon GLUT1 decrease as the cause of cellular death (Figures 3L, 3M, S6G, and S6H). It should be noted that p63 shRNA-induced cell death and GLUT1 attenuation were rescued by ectopic introduction of shRNA-resistant ΔNp63 but not TAp63, validating the predominant role the ΔNp63 isoform plays in modulating SCC GLUT1 expression and maintaining viability (Figure S6I). Of note, pyruvate supplementation in SCC cells failed to rescue GLUT1-knockdown-induced cell death, thereby arguing for the primacy of glucose influx for maintaining antioxidant potential over merely fueling cellular energetic needs (Figure S6J).

In vivo tumor growth of lung SCC HCC2814 was also significantly impaired by doxycycline-inducible ΔNp63 knockdown (Figures 3N, S6K, and S6L). ΔNp63 knockdown tumors exhibited markedly decreased GLUT1 expression and elevated intratumoral oxidative stress as indicated by a significant increase in phosphorylation of DNA damage marker p-H2AX and lipid peroxidation marker 4-hydroxynonenal (4-HNE) staining (Figure 3O). GLUT1 is expressed only in a small population of cells that retain p63 expression in Tet-shΔNp63 tumors, further supporting the dependency of GLUT1 expression on ΔNp63 (Figure S6M). Importantly, NAC supplementation effectively restored tumor growth of ΔNp63-deficient tumors and markedly reduced intratumoral oxidative stress (Figures 3N and 3O). Collectively, these results suggest that p63 essentially contributes to cellular proliferation and survival of SCC by transcriptionally activating GLUT1, thus promoting subsequent glucose influx into NADPH and GSH-generating anabolic pathways to sustain anti-oxidative capacity in SCC.

GLUT1 Rescues Oxidative Stress and Cell Death Induced by p63 Deficiency

We next sought to qualify GLUT1-mediated glucose influx as an essential pro-tumorigenic and/or survival cue driven by oncogenic p63 function. Ectopic overexpression of GLUT1 in p63-deficient SCC cells markedly restored cellular proliferation and viability upon p63 knockdown in lung (HCC2814) and skin (A431) SCC cell lines (Figures 4A, 4B, S7A, and S7B). GLUT1 reconstitution increased glucose uptake, implicating GLUT1 as primarily responsible for glucose influx (Figure 4C), and reduced oxidative stress (Figure 4D) by restoring NADPH and GSH production (Figures 4E and 4F) in p63-deficient SCC cells. Notably, GLUT1 overexpression dramatically restored tumorigenic as

Figure 2. p63 Regulates GLUT1 Expression in SCC

(A) IF staining for GLUT1 (green) and p63 (red) in human SCC tissue samples. Scale bars, 300 μm.

(B) qRT-PCR (left) and immunoblot analyses (right) of p63 and GLUT1 expression in shScr and shp63 lung SCC HCC2814 cells (n = 4).

(C) Representative ICC images (left) and quantification (right) of p63 and GLUT1 expression in shScr or shp63 HCC2814 cells. (n = 3, 5–10 images were captured per group and normalized to nuclei for quantification). Scale bars, 100 μm.

(D) qRT-PCR (left) and immunoblot analyses (right) of ΔNp63 and GLUT1 expression in shScr and shΔNp63 HCC2814 and KYSE70 (n = 4).

(E) qRT-PCR (left) and immunoblot analyses (right) of ΔNp63 and GLUT1 expression in HCC2814 cells overexpressing EGFP or ΔNp63α (n = 3).

(F) Quantification of 2-NBDG uptake in HCC2814 cells overexpressing EGFP or ΔNp63α (n = 3, 8–12 images were captured in each group for quantification).

(G) Publicly available ChIP-seq alignment of p63 binding and H3K27ac on the *SLC2A1* locus. p63 ChIP-seq was performed in HN SCC JHU-029 (GEO: GSE88859) and ENCODE histone mark ChIP-seq was performed in HeLa-S3 (GEO: GSM733684). Homer analysis (Heinz et al., 2010) identifies enriched p63 binding motifs in peak regions (E1–E3) of the *SLC2A1* locus.

(H) ChIP-PCR analysis for endogenous p63 and H3K27ac on the potential p63 binding regions in the intronic enhancer cluster of the *SLC2A1* in HCC2814 and KYSE70. Values represent the average of triplicates ± SEM in a representative experiment. Data represent a minimum of two independent experiments.

(I) Luciferase reporter assay measuring the transcriptional activity of individual enhancers E1, E2, and E3 in shScr or shΔNp63 HCC2814 and KYSE70 cells (n = 3). Luciferase signal is normalized to β-galactosidase activity.

(J) GLUT1 and GLUT3 mRNA expression in CRISPR-Cas9-medated genome editing of the E2 p63-binding enhancer region (n = 3).

All error bars represent the mean ± SEM. ****p < 0.0001, ***p < 0.001, **p < 0.01, *p < 0.05. Two-tailed t test was used unless noted otherwise.

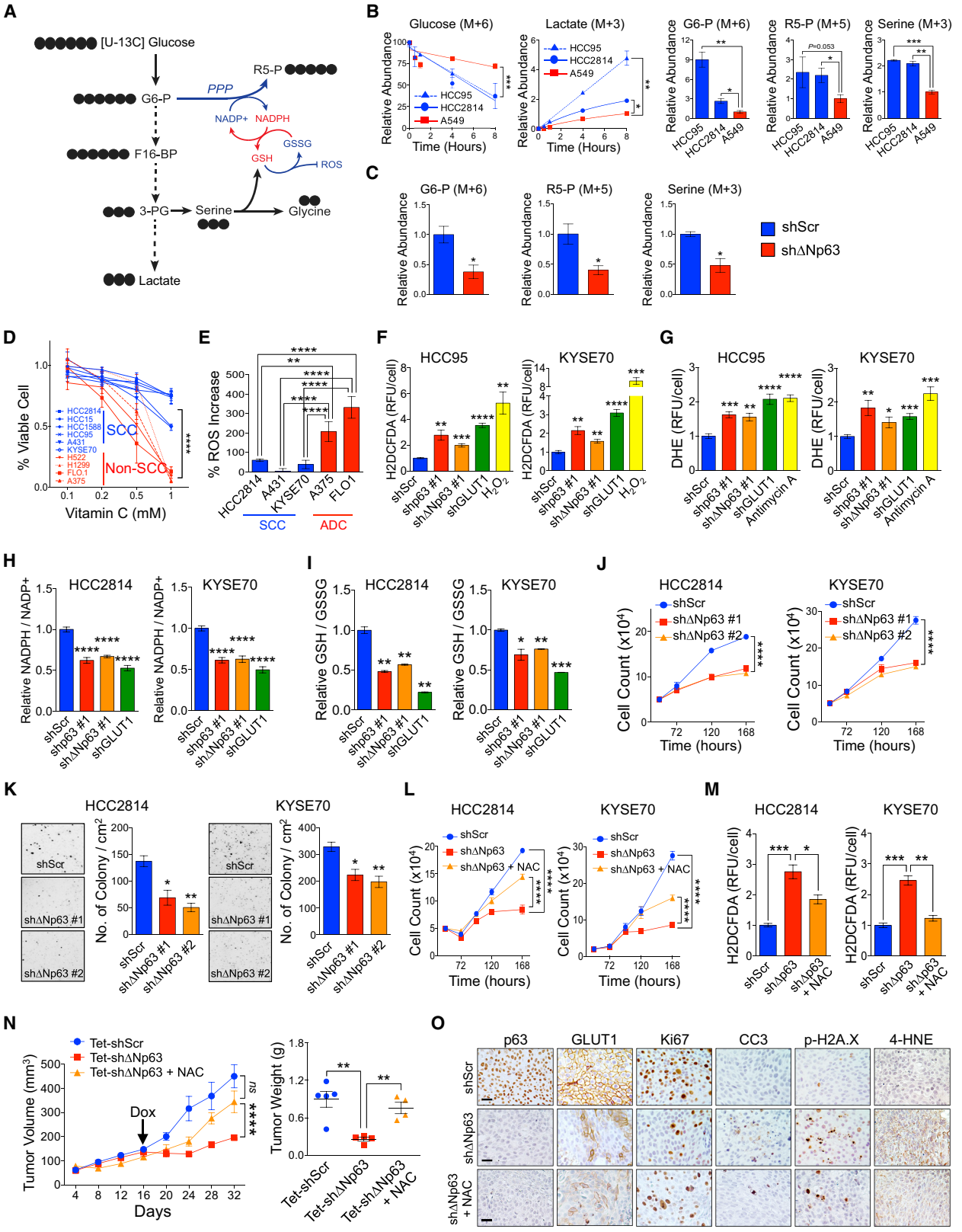

(legend on next page)

well as anti-oxidative capacities of ΔNp63-deficient tumors (Figures 4G and 4H). These results suggest that it is the ΔNp63-knockdown-dependent decrease in GLUT1 that chiefly affects cellular viability.

SOX2 Cooperates with p63 to Transactivate GLUT1 in SCC

TCGA CNV analysis indicates that SOX2 is co-amplified with p63 in up to 40% of human SCCs (Figure S8A). Moreover, a recent study has demonstrated that SOX2 interacts with p63 and jointly occupies genomic loci to promote squamous cancer progression (Watanabe et al., 2014). These findings prompted us to hypothesize that p63 and SOX2 may cooperatively act to induce GLUT1 expression. Indeed, SOX2 knockdown attenuates GLUT1 mRNA and protein expression (Figures 5A, 5B, S8B, and S8C) as well as cellular glucose uptake and lactate production in SCC cell lines (Figures 5C and S8D). Consistent with a previous study, co-immunoprecipitation (coIP) indicates that p63 does indeed interact with SOX2 (Watanabe et al., 2014) (Figure 5D). Notably, our ChIP analysis identified robust SOX2 binding in one of the *SLC2A1* intronic p63 binding enhancer clusters (E2) (Figures 5E, 2G, and S8E). Furthermore, our analysis on global SOX2 occupancy from the publicly available ChIP-seq dataset revealed a strong SOX2 binding signal within E2 where canonical SOX2 and p63 binding sites are co-localized (Perez et al., 2007; Reményi et al., 2003) (Figure 5F). As these results suggest that p63 and SOX2 may form a transcriptional complex in transactivating *SLC2A1*, we sought to determine whether the enhancer binding capacity of one factor is dependent on the other. Intriguingly, SOX2 enhancer binding is markedly attenuated when p63 is knocked down (Figure 5G), whereas p63 sustains its binding capacity regardless of SOX2 levels (Figure S8F) suggesting p63 may play a dominant role in transactivating *SLC2A1* jointly with SOX2. Although further study is required to elucidate the biological implications of this functional interplay, our data argue for crucial cooperation between p63 and SOX2 in promoting GLUT1 expression.

Analogous to p63 inhibition, SOX2 knockdown significantly attenuated NADPH/NADP+ and GSH/GSSG ratios (Figures 5H, 5I, S8G, and S8H), which is associated with an increase in ROS (Figures 5J, S8I, and S8J) and marked decreases in *in vitro* proliferation (Figures 5K and S8K) and cellular transformation capacity (Figure 5L). Ectopic GLUT1 reconstitution upon SOX2 ablation effectively restored cellular proliferation (Figures 5M and 5N), glucose uptake (Figure 5O), and cellular anti-oxidative capacity (Figure 5P), thus implicating SOX2-mediated regulation of GLUT1 specifically in maintaining viability. Collectively, these results suggest that SOX2 regulates GLUT1 expression by transactivating the *SLC2A1* enhancer cooperatively with p63.

Dietary Glucose Restriction Suppresses Human SCC Xenograft Tumor Growth

Given the strict reliance of SCC on glucose for sustaining anti-oxidative capacity and survival, we reasoned that SCC might be highly susceptible to glucose restriction. Thus, we investigated the therapeutic effects of dietary glucose restriction by feeding mice bearing xenograft tumors with a ketogenic diet (0.1% carbohydrate). Xenograft tumor growth of lung SCC (HCC2814 and HCC95) and esophageal SCC (KYSE70) was significantly inhibited upon ketogenic diet as compared to normal chow-fed groups (Figures 6A, S9A, S9B, and S9G). Inhibited tumor growth is associated with a significant reduction in cellular proliferation and increase in apoptosis (Figures 6C, S9D, and S9E). In sharp contrast, ketogenic diet had no effect on the tumor growth of lung ADC, A549, and esophageal ADC, FLO-1 (Figures 6B, 6C, S9C, S9F, and S9G). Importantly, ketogenic diet effectively reduced blood glucose levels, but exerted no adverse effects including hypoglycemia or weight loss (Figures 6A, 6B, S9H, and S9I). Corroborating the *in vitro* results, glucose restriction by ketogenic diet induced oxidative stress in lung SCC xenograft tumors as indicated by a significant increase in p-H2AX and 4-HNE staining (Figures 6C). We also observed increased oxidative stress in SCC tumors treated with glycolytic inhibitor, 2-deoxyglucose (2-DG), or GLUT1 inhibitor, WZB117, as well as shRNA-mediated GLUT1 knockdown, which is associated with significant tumor growth inhibition as we previously reported (Goodwin et al., 2017) (Figure S10A–S10C). Collectively, these results suggest that SCC tumors crucially rely on glucose to maintain anti-oxidative power.

In addition to the restriction of glucose available for SCC cells, reduction of blood glucose can lower blood insulin levels, which

Figure 3. p63/GLUT1 Enhances Anti-oxidative Power in SCC

(A) Schematic representation of uniformly labeled glucose-derived carbons in glucose metabolic pathways.

(B and C) Fates of [U-^{13}C] glucose-derived carbons in glycolysis, PPP, and *de novo* serine biosynthesis in lung SCC HCC95 and HCC2814 and lung ADC A549 (B) and shScr and shΔNp63 HCC2814 (C) cells. Relative ^{13}C abundance of glucose and lactate in the culture media or intracellular glucose-6-phosphage (G6-P), ribose-5-phosphate (R5-P), and serine after 4 h of incubation with [U-^{13}C] glucose were determined by gas chromatography-mass spectrometry (GC/MS). Values represent the average of triplicates ± SEM. Data represent a minimum of two independent experiments.

(D) Cell viability of SCC and non-SCC cell lines cultured in increasing vitamin C concentration for 48 h (n = 4). Two-way ANOVA.

(E) Increase in intracellular ROS levels measured by H_2DCFDA staining in SCC and non-SCC cell lines treated with 1 mM vitamin C for 48 h (n = 3).

(F and G) Relative intracellular ROS level by H_2DCFDA (F) and DHE (G) staining in shScr, shp63, shΔNp63, and shGLUT1 HCC95 and KYSE70 cells (n = 4).

(H and I) Relative intracellular NADPH/NADP+ ratio (H) and GSH/GSSG ratio (I) in shScr, shp63, shΔNp63, and shGLUT1 HCC2814 and KYSE70 cells (n = 3).

(J) *In vitro* proliferation of shScr and shΔNp63 HCC2814 and KYSE70 cells (n = 4). Two-way ANOVA.

(K) Soft agar colony formation assays of shScr and shΔNp63 HCC2814 and KYSE70 cells. Images are representative of three independent experiments. Number of colonies was analyzed after 21 days (n = 3).

(L and M) *In vitro* proliferation (L) of shScr, shΔNp63, and shΔNp63 treated with NAC and intracellular ROS levels (M) measured by H_2DCFDA staining in HCC2814 and KYSE70 cells (n = 3). Two-way ANOVA.

(N and O) Tumor growth (left) and tumor weight (right) (N) and IHC analysis (O) of p63, GLUT1, Ki67, CC3, p-H2A.X, 4-HNE in Tet-inducible shScr (n = 5), shΔNp63 (n = 4), and shΔNp63 treated with NAC (10 g/L) (n = 4) HCC2814 xenograft tumors. Two-way ANOVA. Scale bars, 100 μm. ns, not significant.

All error bars represent the mean ± SEM. ****p < 0.0001, ***p < 0.001, **p < 0.01, *p < 0.05. Two-tailed t test was used unless noted otherwise.

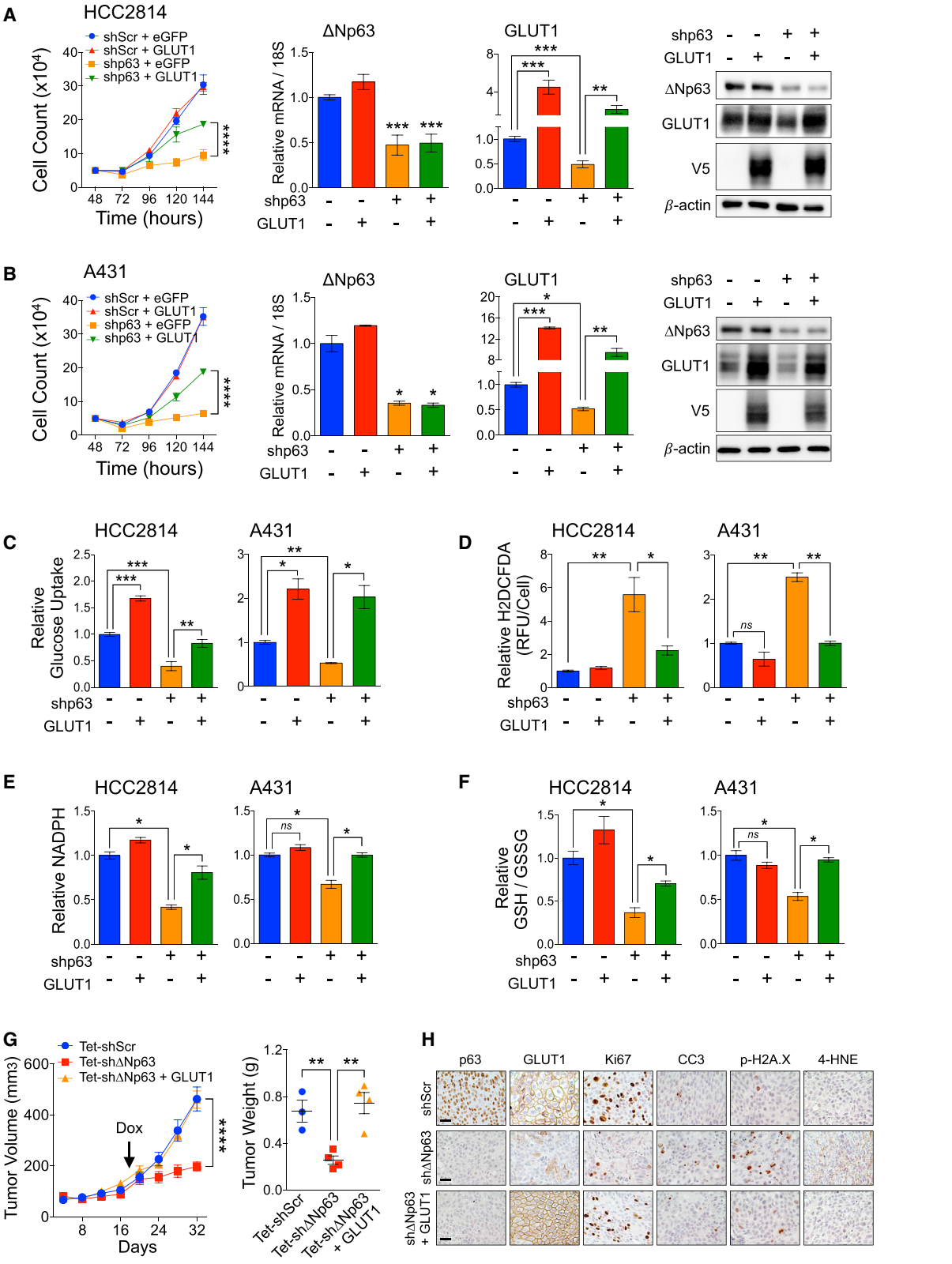

(legend on next page)

may attenuate PI3K/AKT signaling activity in cancer cells and thereby confer synergistic anti-cancer effects. Our recent study and other groups have demonstrated that SCCs exhibit highly activated PI3K/AKT signaling due to the frequent amplification of chromosome 3q26 that contains PIK3CA, a catalytic subunit of the PI3K complex (Goodwin et al., 2017; Yamamoto et al., 2008). Indeed, ketogenic diet resulted in a significant reduction of blood insulin levels (Figures 6A, 6B, and S9H), which is associated with a significant attenuation of AKT signaling in high PIK3CA copy number lung SCC HCC2814 and HCC95 xenograft tumors (Figures 6C and S10D) (Yamamoto et al., 2008). Insulin effectively promoted *in vitro* proliferation and AKT signaling activity of SCC cells indicating that SCC cells respond to insulin (Figure 6D). These results suggest that ketogenic-diet-mediated glucose restriction effectively suppresses *in vivo* tumor growth of SCC by not only perturbing glucose-fueled anti-oxidative defense machinery but also by reducing blood insulin which then suppresses PI3K/AKT signaling in SCC tumors.

Despite significant tumor growth inhibition, there was no tumor regression by ketogenic diet alone. Hence, we sought to determine if a therapeutic combination of ketogenic diet and cisplatin, an alkylating agent and standard chemotherapeutic treatment for SCCs (Dotto and Rustgi, 2016), might achieve more potent therapeutic outcomes by enhancing the cytotoxic effect of cisplatin-mediated ROS burst. Combination of ketogenic diet with cisplatin (5 mg/kg/week) was evidently more effective than a single treatment of either ketogenic diet or cisplatin alone without any noticeable adverse effects (Figures 6E, S11A, and S11D). Accordingly, we detected a marked reduction of proliferation with an increase in apoptosis and intratumoral oxidative stress (Figure S11B). Notably, cisplatin treatment neither affected blood glucose levels nor attenuated PI3K/AKT pathway signaling, thus arguing for the ketogenic-diet-dependent insulin and PI3K/AKT attenuation in SCC tumors (Figures S11B and S11C). Consistent with *in vivo* results, SCC cells cultured in low glucose (1 mM glucose), which mimics ketogenic-diet-mediated glucose restriction, were more susceptible to cisplatin treatment (Figure S11E).

Glucose Restriction Specifically Suppresses SCC in LSL-Kras^{G12D}Lkb1$^{flox/flox}$ LSL-Luc (KL$_{Luc}$) Genetically Engineered Murine Model (GEMM)

We next sought to evaluate the effects of ketogenic diet in the KL$_{Luc}$ mouse model, which develops a full spectrum of NSCLC tumor types including SCC, ADC, and mixed adenosquamous tumors (Ji et al., 2007; Li et al., 2015), envisioning selective sensitivity in SCC tumors. Indeed, KL$_{Luc}$ mice fed with a ketogenic diet exhibited dramatically less SCC tumor development (Figures 7A and 7B), whereas total tumor burden or overall survival was not affected (Figures 7C, 7D, and S12A), indicating that a ketogenic diet pointedly inhibited the development of KL$_{Luc}$ SCC tumors but not ADC tumors. Substantiating the xenograft tumor results, ketogenic diet effectively reduced blood glucose and insulin levels in KL$_{Luc}$ mice (Figures 7E and 7F), which consequently increased oxidative stress and suppressed PI3K/AKT signaling in SCC tumors (Figure 7G), whereas in ADC tumors, oxidative stress or PI3K/AKT signaling was not affected by a ketogenic diet (Figure S12B).

Next, we sought to pharmacologically restrict blood glucose by inhibiting host sodium-glucose co-transporter 2 (SGLT2), which is primarily expressed in the proximal tubules of the kidney and responsible for 90% of renal glucose reabsorption (Wright et al., 2007). Analogous to dietary glucose restriction, treatment with a FDA-approved anti-diabetic SGLT2 inhibitor, canagliflozin (CAG), effectively suppressed SCC tumor development in KL$_{Luc}$ mice (Figures 7A and 7B) and was associated with elevated oxidative stress and suppressed insulin/PI3K/AKT signaling (Figures 7E–7G). Yet, total tumor burden or overall survival was not affected (Figures 7C, 7D, and S12A). Recent studies reported that SGLT2 inhibition exerted anti-cancer effects on pancreatic ductal adenocarcinoma, prostate cancer, astrocytoma, and early stage lung ADC by SGLT2-mediated glucose uptake as SGLT2 appears to be functionally expressed in these cancers (Kepe et al., 2018; Scafoglio et al., 2015; Scafoglio et al., 2018). However, direct SGLT2 inhibition of tumors may not be the cause of cell death in SCC as SGLT2 is not expressed in SCC cell lines (Figures S13A), human SCC tumors (Figure S13B), and KL$_{Luc}$ tumors (Figures S13C–S13E). Consistent with a previous study, we were able to detect SGLT2 expression in premalignant, early stage ADC, but not in advanced ADC tumors in KL$_{Luc}$ mice (Figure S13C) (Scafoglio et al., 2018). It should be noted that CAG was administered when a majority of the tumors were in advanced stages (5-weeks post-adenoviral-cre inhalation), which ensured the effects of CAG on KL$_{Luc}$ tumors were due to inhibition of host SGLT2 primarily in the kidney. Accordingly, *in vitro* SGLT2 inhibition neither affected viability nor glucose uptake in SCC cells (Figures S13F–S13H). Rather, these results suggest that the anti-SCC effects of SGLT2 inhibition are likely due to glucose restriction by systemic modulation and an associated suppression of insulin/PI3K/AKT signaling in cancer cells.

To further validate the necessity of glucose in SCC survival and tumor growth, we genetically ablated *Slc2a1* in KL$_{Luc}$ mice (*LSL-Kras^{G12D}Lkb1$^{flox/flox}$Glut1$^{flox/flox}$*, KL GLUT1-knockout [KO]) (Young et al., 2011). *Slc2a1* deletion dramatically decreased SCC tumors (Figures 7H and 7I), yet total tumor burden was not affected (Figure 7J), again indicating that GLUT1 plays pivotal roles in SCC tumorigenesis but remains

Figure 4. GLUT1 Rescues Oxidative Stress and Cell Death Induced by p63 Inhibition

(A and B) *In vitro* proliferation, qRT-PCR, and immunoblot analysis of ΔNp63, GLUT1 and V5-tag expression of shScr and shp63 lung SCC HCC2814 (A) and skin SCC A431 (B) cells ectopically overexpressing EGFP or GLUT1 (n = 3). Two-way ANOVA.

(C–F) Relative glucose uptake (C), intracellular ROS (D), intracellular NADPH (E), and GSH/GSSG ratio (F) in shScr and shp63 HCC2814 (left) and A431 (right) ectopically overexpressing EGFP or GLUT1 (n = 3).

(G and H) Tumor growth (left) and tumor weight (right) (G) and IHC analysis (H)of p63, GLUT1, Ki67, CC3, p-H2AX, 4-HNE in Tet-inducible shScr (n = 3), shΔNp63 (n = 4), and shΔNp63 overexpressing GLUT1 (n = 4) HCC2814 xenograft tumors. Two-way ANOVA. Scale bars, 100 μm.

All error bars represent the mean ± SEM. ****p < 0.0001, ***p < 0.001, **p < 0.01, *p < 0.05. Two-tailed t test was used unless noted otherwise.

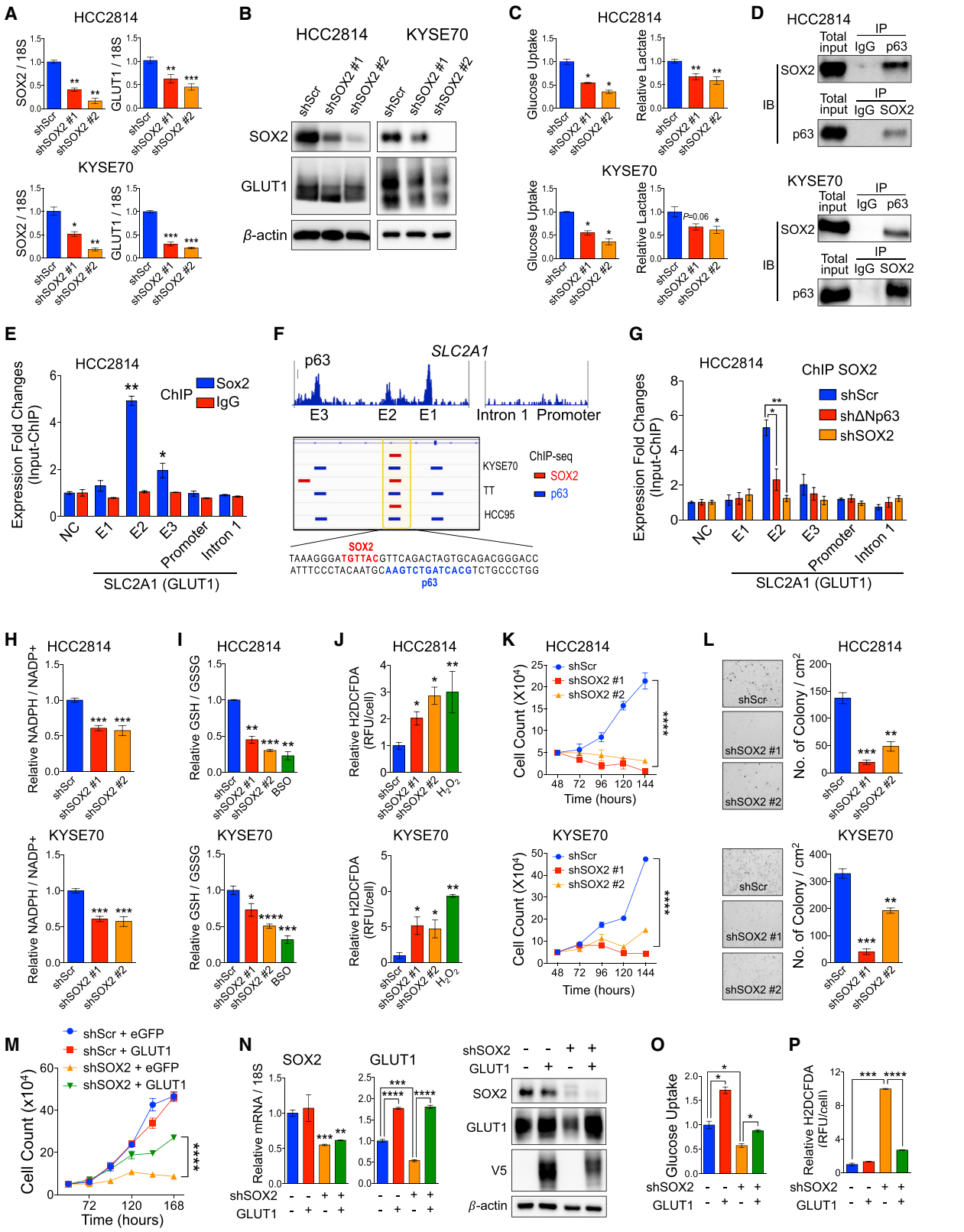

(legend on next page)

dispensable for ADC tumors. It should be noted that a small number of SCC tumors identified in KL GLUT1-KO mice do express GLUT1 (Figures 7K and S14A) presumably due to incomplete Cre recombination of the floxed *Slc2a1* gene in those tumors, further corroborating the essentiality of GLUT1 in SCC tumorigenesis. Collectively, these results support our model that glucose restriction can be an effective therapeutic strategy for SCC tumors.

High Blood Glucose Correlates with Poor Prognosis in SCC Patients

To verify the clinical relevance of SCC glucose reliance, we performed Kaplan-Meier survival analysis with a cohort of lung and esophageal cancer patients to examine the prognostic value of random blood glucose (RBG) levels in SCC patients (Ziemer et al., 2008). We identified a robust correlation between high random blood glucose (>120 mg/dL) and poor survival rate in lung and esophageal SCC patients (Figures 7L and 7M), but no such correlation was found among lung ADC patients (Figure 7N). The 120-mg/dL cutoff of random blood glucose has proven to provide over 90% specificity for detection of glucose intolerance in humans (Ziemer et al., 2008) and recently has shown to be associated with poor prognosis in breast cancer patients (Monzavi-Karbassi et al., 2016). Notably, none of these patients have been diagnosed with diabetes, indicating that they have not been exposed to any anti-diabetic agents. These results are accordant with a previous epidemiological study demonstrating a higher glycemic index among lung SCC patients (Melkonian et al., 2016), thus highlighting the potential prognostic feasibility of circulating blood glucose concentrations in SCC patients.

DISCUSSION

Targeting altered glucose metabolism in cancer cells has resulted in varied and unsatisfactory outcomes (Luengo et al., 2017). Among multiple factors preventing effective therapeutic responses, a poorly understood tumor-intrinsic metabolic heterogeneity across different cancers may preclude effective therapeutic strategies to target cancer metabolism. Here, we uncover a previously unrecognized metabolic reliance and vulnerability distinctively embedded across all SCCs, in which the major glucose transporter GLUT1 is exceptionally overexpressed through the squamous lineage-specific transcriptional network, p63 and SOX2. Enhanced GLUT1 expression is linked to an exquisite reliance on glucose for survival and tumor growth in SCC. This strongly argues that hyperactive GLUT1 activity and dramatically enhanced glucose influx is not a uniform metabolic hallmark of all cancers but rather a potent and unique characteristic of SCC, thereby rendering SCC the most susceptible tumor type to glucose restriction and may present an actionable therapeutic window.

Although recent studies have shown that SCC exhibits heightened cellular anti-oxidative capacity through p63- and NRF2-mediated transcriptional control of genes involved in the PPP, *de novo* serine biosynthesis, and GSH metabolism (DeNicola et al., 2015; Mitsuishi et al., 2012; Wang et al., 2017), robust glucose influx is equally crucial to metabolically fuel these pathways to generate redox power. Our study establishes a model in which ΔNp63 in cooperation with SOX2 metabolically couples high glucose influx and anti-oxidative pathways by transcriptional upregulation of GLUT1. Accordingly, inhibition of ΔNp63 or SOX2 expression deprived cellular NADPH and GSH pools and impaired cellular proliferation and viability of SCC (Figure 3). Importantly, overexpression of GLUT1 successfully restored glucose uptake, anti-oxidative capacity, and viability of p63-deficient SCC cells (Figure 4), supporting the essential contribution of ΔNp63/SOX2-GLUT1-mediated glucose influx to redox homeostasis within SCC. Recently, hexokinase 2 (HK2) has been identified as a direct ΔNp63 target gene in human keratinocytes and has been shown to regulate mitochondrial ROS generation (Viticchiè et al., 2015). As HK2 catalyzes the first step of glycolysis producing glucose-6-phosphate, which is diverted into the PPP, the biological significance of ΔNp63 in directing glucose utilization into maintaining redox pools is further emphasized.

Strong co-occupancy of p63 and H3K27ac in the second intron region of the *SLC2A1* gene is corroborated with a recent study demonstrating that more than half of all genomic p63

Figure 5. SOX2 Regulates GLUT1 Expression

(A and B) qRT-PCR (A) and immunoblot (B) analyses of SOX2 and GLUT1 expression in shScr and shSOX2 HCC2814 and KYSE70 cells (n = 3).

(C) Quantification of 2-NBDG uptake (left) and extracellular lactate (right) in shScr and shSOX2 HCC2814 and KYSE70 cells (n = 3, 8–12 images were captured in each group for quantification).

(D) CoIP analysis of the interaction between endogenous SOX2 and p63 in HCC2814 and KYSE70 cells. Immunoglobulin G (IgG) was used as a negative control.

(E) ChIP-PCR analysis for endogenous SOX2 on potential p63 binding regions in the intronic enhancer cluster of the *SLC2A1* gene in HCC2814 cells. Values represent the average of triplicates ± SEM in a representative experiment. Data represent a minimum of two independent experiments.

(F) Analysis on publicly available ChIP-seq of SOX2 (red bars) and p63 (blue bars) occupancy in the *SLC2A1* intronic enhancer cluster in esophageal SCC lines KYSE70 and TT (Watanabe et al., 2014) and lung SCC line HCC95 (GEO: GSE46837).

(G) ChIP-PCR analysis for endogenous SOX2 on potential p63 binding regions in the intronic enhancer cluster of the *SLC2A1* gene in shScr, shΔNp63, and shSOX2 HCC2814 cells. Values represent the average of triplicates ± SEM in a representative experiment. Data represent a minimum of two independent experiments.

(H–J) Relative intracellular NADPH/NADP+ ratio (H), GSH/GSSH ratio (I), and intracellular ROS (J) in shScr and shSOX2 HCC2814 and KYSE70 cells (n = 3).

(K) *In vitro* proliferation of shScr and shSOX2 HCC2814 and KYSE70 cells (n = 3). Two-way ANOVA.

(L) Soft agar colony formation assays of shScr and shSOX2 HCC2814 and KYSE70 cells. Images are representative of three independent experiments. Number of colonies was analyzed after 21 days (n = 3).

(M) *In vitro* proliferation of shScr and shSOX2 HCC2814 cells ectopically overexpressing EGFP or GLUT1 (n = 3). Two-way ANOVA.

(N) qRT-PCR (left) and immunoblot (right) analysis of SOX2, GLUT1 and V5-tag expression in shScr and shSOX2 HCC2814 cells ectopically overexpressing EGFP or GLUT1 (n = 3).

(O and P) Relative 2-NBDG uptake (O), intracellular ROS levels (P) in shScr, and shSOX2 HCC2814 cells ectopically overexpressing EGFP or GLUT1 (n = 3).

All error bars represent the mean ± SEM. ****p < 0.0001, ***p < 0.001, **p < 0.01, *p < 0.05. Two-tailed t test was used unless noted otherwise.

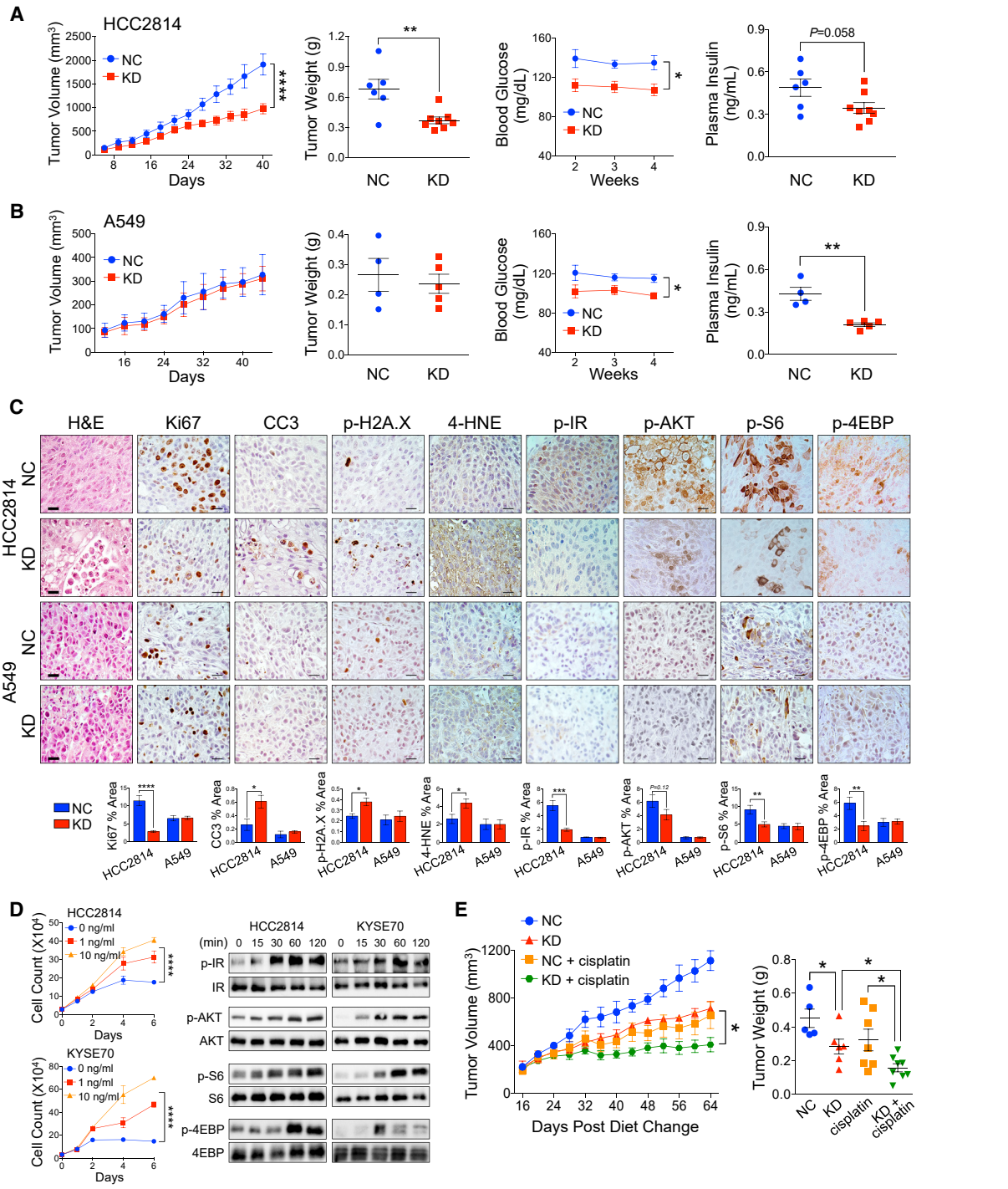

Figure 6. Ketogenic Diet Suppresses SCC Growth *In Vivo*

(A and B) Xenograft tumor growth, tumor weight, and blood glucose and plasma insulin levels of lung SCC HCC2814 (NC, n = 6; KD, n = 8) (A) and lung ADC A549 (NC, n = 4; KD, n = 5) (B) fed with normal chow (NC) as control or ketogenic diet (KD). Two-way ANOVA.

(C) IHC analysis (top) and quantification (bottom) of Ki67, CC3, p-H2AX, 4-HNE, p-IR, p-AKT, p-S6, and p-4EBP in NC (HCC2814, n = 6; A549, n = 4)- and KD (HCC2814, n = 8; A549, n = 5)-fed xenograft tumors. A total of 5–0 images in each tumor were captured and analyzed for quantification. Scale bars, 100 μm.

(D) *In vitro* proliferation (left) and immunoblot analysis (right) of p-IR, IR, p-AKT, AKT, p-S6, S6, p-4EBP, and 4-EBP expression of HCC2814 cells treated with insulin (0–10 ng/mL) (n = 3). Two-way ANOVA.

(E) Tumor growth (left) and tumor weight (right) of HCC2814 xenograft tumors treated with NC alone (NC, n = 5) as control, NC with cisplatin (NC+cisplatin, n = 7), KD alone (KD, n = 6), and KD with cisplatin (KD+cisplatin, n = 8). Two-way ANOVA.

All error bars represent the mean ± SEM. ****p < 0.0001, ***p < 0.001, **p < 0.01, *p < 0.05. Two-tailed t test was used unless noted otherwise.

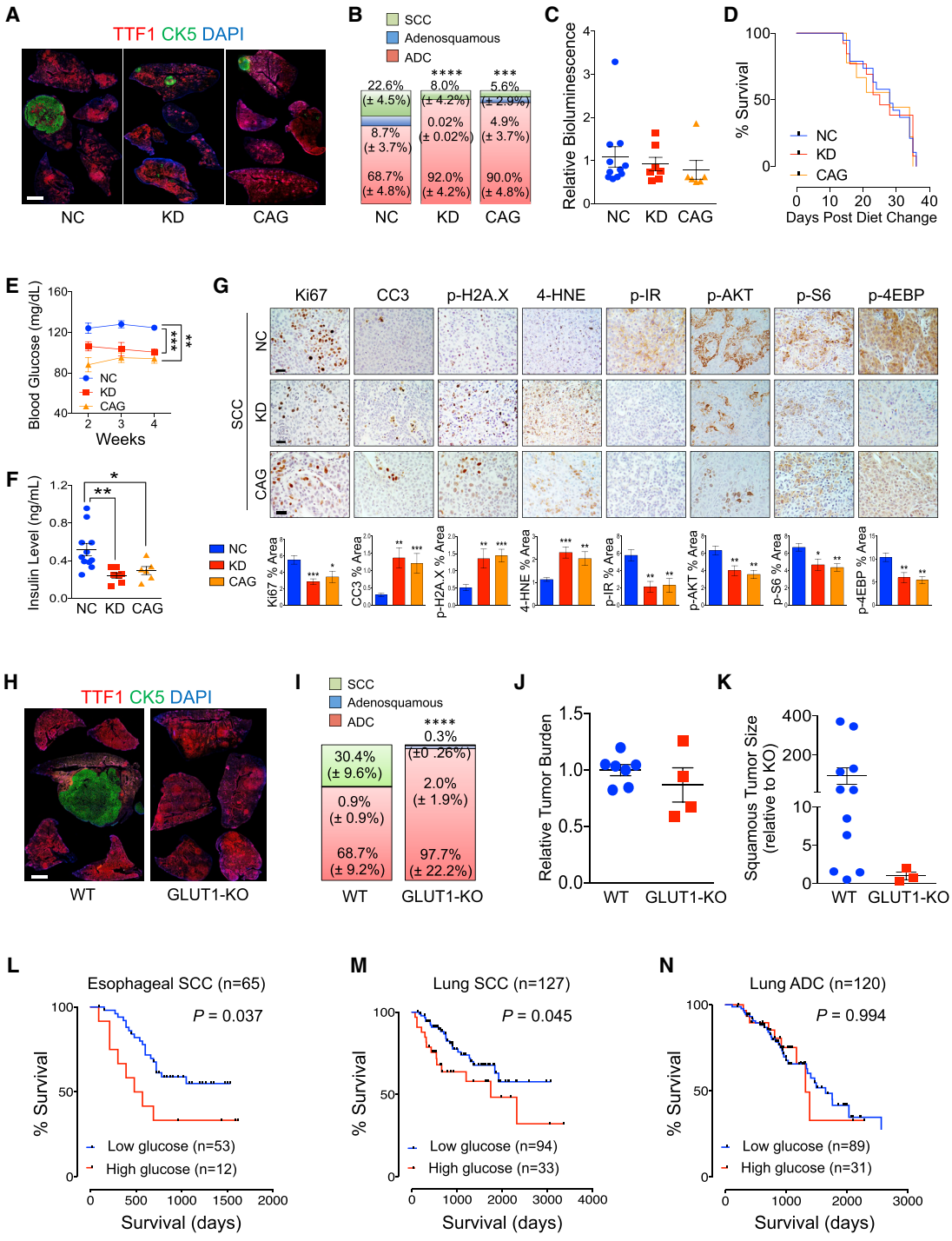

Figure 7. Dietary, Pharmacological, and Genetic Glucose Restriction Suppresses KL_{Luc} SCC Tumor Development

(A and B) Representative thyroid transcription factor-1 (TTF-1; ADC marker) and CK5 (SCC marker) IF images (A) and quantification of SCC, adenosquamous, and ADC tumor types determined by histopathological as well as IHC evaluation of TTF-1/CK5 (B) in KL_{Luc} mice fed with normal chow (NC, n = 11), ketogenic diet (KD, n = 7), or canagliflozin (CAG, n = 6). Chi-square test. Scale bar, 2.5 mm.

(C) Total tumor burden of KL_{Luc} mice analyzed by *in vivo* bioluminescence analysis at 11 weeks post intratracheal injection of adenovirus-Cre (NC, n = 11; KD, n = 7; CAG, n = 6).

(D) Survival analysis of KL_{Luc} mice fed with NC (n = 11), KD (n = 7), or CAG (n = 6).

(E) Blood glucose levels in KL_{Luc} mice fed with NC (n = 11), KD (n = 7), or CAG (n = 6). Two-way ANOVA.

(F) Plasma insulin concentration in KL_{Luc} mice fed with NC (n = 11), KD (n = 7), or CAG (n = 6).

(legend continued on next page)

binding regions are epigenetically marked by an active enhancer marker, H3K27ac, and p63/H3K27ac co-occupied sites were identified as transcriptionally active sites (Kouwenhoven et al., 2015). Given that functional implications of enhancers within introns remain poorly understood, investigating 3D chromatin folding and physical association of the potential p63 binding enhancer cluster with the promoter of the *SLC2A1* gene will be critical to validate the p63 binding enhancer function (Rao et al., 2014). Intriguingly, our study further identified that SOX2 regulates GLUT1 expression. Although the precise molecular mechanism by which p63 and SOX2 may interact to transactivate GLUT1 remains to be fully elucidated, our results indicate that SOX2 transactivates one of the p63 binding enhancers (E2) in the *SLC2A1* gene suggesting the bona fide cooperative regulatory relationships between p63 and SOX2. Co-occupancy of p63 and SOX2 in the *SLC2A1* intronic enhancer cluster was confirmed by analysis on a recent genome-wide p63 and SOX2 ChIP-seq study (Saladi et al., 2017; Watanabe et al., 2014). Moreover, these studies indicated that genomic SOX2 binding in SCC cell lines significantly differs from that in embryonic stem cells suggesting that its oncogenic functions in SCC are defined by tissue-specific transcriptional binding partners such as p63, especially considering our finding that SOX2 may only bind *SLC2A1* in the presence of p63 (Figures 5G and S8F) (Watanabe et al., 2014).

Strict reliance of SCC on glucose influx for redox homeostasis and survival provides the rationale to evaluate glucose restriction as a potential therapeutic strategy for SCCs (Allen et al., 2014). Notably, tumor growth inhibition by ketogenic diet or host SGLT2 inhibition was only evident in SCC tumors, whereas glucose restriction neither affected tumor growth nor intratumoral ROS levels of non-SCC tumors (Figures 6, 7, and S9). These findings are in accordance with previous studies revealing that a ketogenic diet enhanced anti-cancer effects when combined with chemotherapy or radiation, yet ketogenic diet alone did not show any growth inhibitory effects on H292 and A549 lung cancer xenograft tumors, which are both of non-squamous origin (Allen et al., 2013). These results highlight the necessity of better understanding intrinsic heterogeneity in glucose reliance across cancer types, which can be exploited for more precise targeted metabolic therapy. Our results, however, cannot completely exclude the possibility that a ketogenic diet or SGLT2 inhibitors may affect SCC metabolism and tumor growth independent of glucose- and/or insulin-mediated effects (Shukla et al., 2014). For instance, recent studies have shown that CAG may target mitochondrial complex I and glutamate dehydrogenase, thereby activating adenosine monophosphate-activated protein kinase (AMPK) and altering amino acid metabolism (Hawley et al., 2016; Secker et al., 2018; Villani et al., 2016). Moreover, ketone bodies have been determined to promote, rather than attenuate, tumor progression of BRAF V600E melanoma and leukemia cells by enhancing the ability of BRAF V600E to activate MEK1-ERK signaling (Kang et al., 2015). Thus, further studies are needed to elucidate the functional implications of CAG and ketone bodies in intrinsic SCC-associated metabolic or oncogenic signaling pathways.

In addition to restriction of available glucose for cancer cells, decreased blood glucose subsequently reduces blood insulin levels. Because PI3K/AKT is a downstream target of canonical insulin signaling, reduced blood glucose levels can attenuate insulin-activated PI3K/AKT signaling in SCC. Importantly, SCC is among cancer types exhibiting highly activated PI3K/AKT signaling due to amplified PIK3CA by genomic amplification of chromosome 3q26 that also contains p63 and SOX2 (Yamamoto et al., 2008). Indeed, our data demonstrate a significant reduction of AKT signaling in ketogenic-diet-fed or CAG-treated SCC tumors but not in A549 ADC or KL ADC tumors, which have considerably less PI3K/AKT activity (Figures 6C, 7G, and S12B). Intriguingly, recent evidence has shown that ketogenic diet and SGLT2 inhibition enhanced the efficacy of PI3K inhibitors by blocking glucose-insulin feedback that is caused by compensatory insulin elevation in response to systemic PI3K inhibition (Hopkins et al., 2018). These results support our model that glucose restriction suppresses intrinsic PI3K/AKT signaling in SCC by reducing blood insulin levels. Our earlier study and others have demonstrated that PI3K/AKT signaling enhances glucose uptake and retention by promoting GLUT1 expression and translocation to the plasma membrane as well as increasing HK2 activity (Rathmell et al., 2003). Therefore, inhibition of insulin/PI3K/AKT signaling in ketogenic-diet-fed or CAG-treated mice may reduce GLUT1 transmembrane localization and HK2 activity in SCC tumors that further restricts glucose uptake and utilization.

A strong correlation between high random blood glucose and worse survival of SCC patients highlights the clinical relevance of SCC-specific strict glucose reliance and further implicates the potential efficacy of glucose restriction in attenuating SCC tumor growth. These results imply that hyperglycemia per se may promote tumorigenic progression and survival of SCC tumors and impede effective therapeutic action resulting in poor prognosis. In light of these findings, it will be critical to determine whether diabetic patients have an increased risk of SCC.

This study presents a viable and potentially rapidly translatable treatment paradigm in targeting squamous cancers precisely not by direct inhibition but modulating metabolism at a systemic level. Cancer cells depend on growth factor availability

(G) Representative IHC images (top) and quantification of % area (right) of Ki67, CC3, p-H2AX, 4-HNE, p-IR, p-AKT, p-S6, and p-4EBP in KL_{Luc} SCC tumors fed with NC (n = 11), KD (n = 7), or CAG (n = 6). A total of 5–10 images in each tumor were captured and analyzed for quantification. Scale bars, 100 μm.
(H–J) Representative TTF-1 and CK5 IF images (H), quantification of individual tumor types (I), and total tumor burden determined by histological analysis of H&E-stained tumor tissues (J) in wild type (*LSL-Kras*^{G12D}; *Lkb1*$^{flox/flox}$; *LSL-Luc*, WT, n = 7) and GLUT1 knockout (*LSL-Kras*^{G12D}; *Lkb1*$^{flox/flox}$; *LSL-Luc; GLUT1*$^{flox/flox}$, GLUT1-KO, n = 4) KL_{Luc} mice. Chi-square test. Scale bar, 2.5 mm.
(K) Comparison of individual SCC tumor size of WT (n = 7) and GLUT1-KO (n = 4) KL_{Luc} mice.
(L–N) Kaplan-Meier survival analysis comparing high and low random blood glucose (RGB) levels in the esophageal SCC (n = 65) (L), lung SCC (n = 127) (M), and lung ADC (n = 120) (N) patient cohorts. High and low RGB groups were separated by 120 mg/dL. Significance was determined with the log-rank test.
All error bars represent the mean ± SEM. ****p < 0.0001, ***p < 0.001, **p < 0.01, *p < 0.05. Two-tailed t test was used unless noted otherwise.

and proliferative signaling pathways such as PI3K/AKT to activate nutrient uptake and subsequent metabolic processes to drive growth (Palm and Thompson, 2017). Thus, metabolic processes and growth signaling fundamentally converge to drive proliferation. In light of our study demonstrating the strict glucose reliance of SCC driven by the squamous lineage-specific p63 and SOX2 transcriptional complex, we envision that p63/SOX2-GLUT1 and PI3K/AKT signaling, among other pathways, remain central in an oncogenic network driving antioxidant defense and proliferation that is deeply linked to SCC etiology and identity. By restricting glucose not only is nutrient acquisition affected but also a profound synergistic effect suppressing metabolic, antioxidant, and tumor-intrinsic growth signaling pathways essential for squamous oncogenicity may be exerted and chemotherapeutic resistance potentially precluded. Given that SGLT2 inhibition has been well tolerated without clinical hypoglycemia in non-diabetic humans and mice treated with CAG (Devineni et al., 2015) (Figures 7E and S13I), repurposing FDA-approved anti-diabetic SGLT2 inhibitors may be tractable and rapidly translatable as a safe and effective therapeutic strategy in combination with existing treatments for squamous cancers and may hold significant promise in improving therapeutic outcomes for SCC patients.

STAR★METHODS

Detailed methods are provided in the online version of this paper and include the following:

- KEY RESOURCES TABLE
- LEAD CONTACT AND MATERIALS AVAILABILITY
- EXPERIMENTAL MODEL AND SUBJECT DETAILS
  - Human Tumor Samples and Survival Analyses
  - Mice
  - Cell Line
- METHOD DETAILS
  - *In Vivo* Tumor Xenograft Experiments
  - *In Vivo* KL_{Luc} Mice Experiments
  - Ketogenic Diet and Canagliflozin Treatment
  - Blood Glucose and Insulin Measurement
  - Immunoblot Analysis
  - mRNA Quantification
  - *In Vitro* Metabolic Analysis
  - *In vitro* ROS Measurement
  - U-^{13}C Glucose Tracing and GC-MS Metabolomics
  - Immunoprecipitation (IP)
  - Chromatin Immunoprecipitation (ChIP)
  - CRISPR-Cas9 Genome Editing
  - shRNA Knockdown
  - Luciferase Assays
  - Stable Cell Lines
  - Immunocytochemistry
  - Immunohistochemistry and Immunofluorescence Analysis
  - Soft Agar Colony Formation Analysis
  - TCGA Analyses
- QUANTIFICATION AND STATISTICAL ANALYSIS
- DATA AND CODE AVAILABLITY

SUPPLEMENTAL INFORMATION

Supplemental Information can be found online at https://doi.org/10.1016/j.celrep.2019.07.027.

ACKNOWLEDGMENTS

We thank An Hong Nguyen for technical assistance. We thank David Sidransky (Johns Hopkins University), Vlad Sandulache (Baylor College of Medicine), Ralph Weichselbaum (University of Chicago), Jeffrey Meyers (MD Anderson Cancer Center), John Minna, Richard Wang, David Wang, and Wei Zhang (University of Texas Southwestern Medical Center), and Zui Pan (University of Texas at Arlington) for providing cell lines. This work was supported by American Lung Association, United States, LCD-400239, DOD, United States, W81XWH-18-1-0439, CPRIT, United States, RP180670, and NIH, United States, 5R21CA208746 and P50CA70907 to J.K.; CPRIT RP160089 and NIH R35CA220449 to R.J.D.; Japan Agency for Medical Research and Development Grants-in Aid, P-CREATE, AMED, Japan, to M.I.; NIH K25EB017222 and R01EB025841 and CPRIT RP180670 to K.H.; NIH R01CA210439, R01CA216853, P50CA127297, and P01CA217798 to P.K.S.; NIH P50CA70907 to J.D.M.; American Cancer Society, United States, RSG-16-234-01-TBG to D.B.S.; NIH/NCATS UCLA Clinical & Translational Science Institute KL2 Translational Science Award, United States, UL1TR001881, American Cancer Society RSG-17-003-01-CCE, Tobacco-Related Disease Research Program, United States, 2016TRDRP0IR00000143977, and STOP Cancer Foundation Seed Grant, United States, to C.S.; National Research Foundation of Korea, South Korea, NRF-2016R1A1A1A-05005315 to S.Y.L.; and NSF, United States, CAREER 1351354 and NSF 1361355 to L.B. and C.N.

AUTHOR CONTRIBUTIONS

Conception and design, M.H. and J.K.; Development of methodology, M.-H.H., Y.J.K, C.N., J.G., S.Y.L., V.S., P.K.S., L.B., K.H., Z.X., and M.I.; Investigation and data acquisition, M.-H.H., J.G., Y.J.K., J.H.C., M.A.A., M.P., H.G., C.N., H.D., S.M., J.K.K., M.C., M.K.K., J.Y.J., S.Y.L., B.F., and Z.X.; Data analysis and interpretation, M.-H.H., J.G., Y.J.K., J.H.C., C.N., M.C., M.K.K., J.Y.J., S.Y.L., V.S., Z.X., K.H., C.S., D.B.S., L.B., J.K., R.J.D., T.H.K., and J.K.; Technical and material support, B.F., E.D.A., J.D.M., P.K.S., J.K., M.I., R.J.D., and T.H.K.; Writing and revision of the manuscript, M.H., J.H.C., J.G., and J.K.; Study supervision, J.K.

DECLARATION OF INTERESTS

R.J.D. is an advisor for Agios Pharmaceuticals. J.D.M. receives licensing fees for lung cancer cell lines from the NCI and University of Texas Southwestern Medical Center.

Received: February 22, 2019
Revised: June 17, 2019
Accepted: July 11, 2019
Published: August 13, 2019

REFERENCES

Allen, B.G., Bhatia, S.K., Buatti, J.M., Brandt, K.E., Lindholm, K.E., Button, A.M., Szweda, L.I., Smith, B.J., Spitz, D.R., and Fath, M.A. (2013). Ketogenic diets enhance oxidative stress and radio-chemo-therapy responses in lung cancer xenografts. Clin. Cancer Res. *19*, 3905–3913.

Allen, B.G., Bhatia, S.K., Anderson, C.M., Eichenberger-Gilmore, J.M., Sibenaller, Z.A., Mapuskar, K.A., Schoenfeld, J.D., Buatti, J.M., Spitz, D.R., and Fath, M.A. (2014). Ketogenic diets as an adjuvant cancer therapy: History and potential mechanism. Redox Biol. *2*, 963–970.

Bao, X., Rubin, A.J., Qu, K., Zhang, J., Giresi, P.G., Chang, H.Y., and Khavari, P.A. (2015). A novel ATAC-seq approach reveals lineage-specific reinforcement of the open chromatin landscape via cooperation between BAF and p63. Genome Biol. *16*, 284.

Bardeesy, N., Sinha, M., Hezel, A.F., Signoretti, S., Hathaway, N.A., Sharpless, N.E., Loda, M., Carrasco, D.R., and DePinho, R.A. (2002). Loss of the Lkb1 tumour suppressor provokes intestinal polyposis but resistance to transformation. Nature *419*, 162–167.

Bass, A.J., Watanabe, H., Mermel, C.H., Yu, S., Perner, S., Verhaak, R.G., Kim, S.Y., Wardwell, L., Tamayo, P., Gat-Viks, I., et al. (2009). SOX2 is an amplified lineage-survival oncogene in lung and esophageal squamous cell carcinomas. Nat. Genet. *41*, 1238–1242.

Cancer Genome Atlas Research Network (2012). Comprehensive genomic characterization of squamous cell lung cancers. Nature *489*, 519–525.

Cancer Genome Atlas Research Network (2014). Comprehensive molecular characterization of urothelial bladder carcinoma. Nature *507*, 315–322.

Cancer Genome Atlas; Research Network. (2015). Comprehensive genomic characterization of head and neck squamous cell carcinomas. Nature *517*, 576–582.

Cancer Genome Atlas Research Network; Albert Einstein College of Medicine; Analytical Biological Services; Barretos Cancer Hospital; Baylor College of Medicine; Beckman Research Institute of City of Hope; Buck Institute for Research on Aging; Canada's Michael Smith Genome Sciences Centre; Harvard Medical School; Helen F. Graham Cancer Center &Research Institute at Christiana Care Health Services; HudsonAlpha Institute for Biotechnology; ILSbio, LLC; Indiana University School of Medicine; Institute of Human Virology; Institute for Systems Biology; International Genomics Consortium; Leidos Biomedical; Massachusetts General Hospital; McDonnell Genome Institute at Washington University; Medical College of Wisconsin; Medical University of South Carolina; Memorial Sloan Kettering Cancer Center; Montefiore Medical Center; NantOmics; National Cancer Institute; National Hospital, Abuja, Nigeria; National Human Genome Research Institute; National Institute of Environmental Health Sciences; National Institute on Deafness &Other Communication Disorders; Ontario Tumour Bank, London Health Sciences Centre; Ontario Tumour Bank, Ontario Institute for Cancer Research; Ontario Tumour Bank, The Ottawa Hospital; Oregon Health &Science University; Samuel Oschin Comprehensive Cancer Institute, Cedars-Sinai Medical Center; SRA International; St Joseph's Candler Health System; Eli &Edythe L. Broad Institute of Massachusetts Institute of Technology &Harvard University; Research Institute at Nationwide Children's Hospital; Sidney Kimmel Comprehensive Cancer Center at Johns Hopkins University; University of Bergen; University of Texas MD Anderson Cancer Center; University of Abuja Teaching Hospital; University of Alabama at Birmingham; University of California, Irvine; University of California Santa Cruz; University of Kansas Medical Center; University of Lausanne; University of New Mexico Health Sciences Center; University of North Carolina at Chapel Hill; University of Oklahoma Health Sciences Center; University of Pittsburgh; University of São Paulo, Ribeir ão Preto Medical School; University of Southern California; University of Washington; University of Wisconsin School of Medicine &Public Health; Van Andel Research Institute; Washington University in St Louis (2017a). Integrated genomic and molecular characterization of cervical cancer. Nature *543*, 378–384.

Cancer Genome Atlas Research Network; Analysis Working Group: Asan University; BC Cancer Agency; Brigham and Women's Hospital; Broad Institute; Brown University; Case Western Reserve University; Dana-Farber Cancer Institute; Duke University; Greater Poland Cancer Centre; Harvard Medical School; Institute for Systems Biology; KU Leuven; Mayo Clinic; Memorial Sloan Kettering Cancer Center; National Cancer Institute; Nationwide Children's Hospital; Stanford University; University of Alabama; University of Michigan; University of North Carolina; University of Pittsburgh; University of Rochester; University of Southern California; University of Texas MD Anderson Cancer Center; University of Washington; Van Andel Research Institute; Vanderbilt University; Washington University; Genome Sequencing Center: Broad Institute; Washington University in St. Louis; Genome Characterization Centers: BC Cancer Agency; Broad Institute; Harvard Medical School; Sidney Kimmel Comprehensive Cancer Center at Johns Hopkins University; University of North Carolina; University of Southern California Epigenome Center; University of Texas MD Anderson Cancer Center; Van Andel Research Institute; Genome Data Analysis Centers: Broad Institute; Brown University; Harvard Medical School; Institute for Systems Biology; Memorial Sloan Kettering Cancer Center; University of California Santa Cruz; University of Texas MD Anderson Cancer Center; Biospecimen Core Resource: International Genomics Consortium; Research Institute at Nationwide Children's Hospital; Tissue Source Sites: Analytic Biologic Services; Asan Medical Center; Asterand Bioscience; Barretos Cancer Hospital; BioreclamationIVT; Botkin Municipal Clinic; Chonnam National University Medical School; Christiana Care Health System; Cureline; Duke University; Emory University; Erasmus University; Indiana University School of Medicine; Institute of Oncology of Moldova; International Genomics Consortium; Invidumed; Israelitisches Krankenhaus Hamburg; Keimyung University School of Medicine; Memorial Sloan Kettering Cancer Center; National Cancer Center Goyang; Ontario Tumour Bank; Peter MacCallum Cancer Centre; Pusan National University Medical School; Ribeirão Preto Medical School; St. Joseph's Hospital &Medical Center; St. Petersburg Academic University; Tayside Tissue Bank; University of Dundee; University of Kansas Medical Center; University of Michigan; University of North Carolina at Chapel Hill; University of Pittsburgh School of Medicine; University of Texas MD Anderson Cancer Center; Disease Working Group: Duke University; Memorial Sloan Kettering Cancer Center; National Cancer Institute; University of Texas MD Anderson Cancer Center; Yonsei University College of Medicine; Data Coordination Center: CSRA Inc.; Project Team: National Institutes of Health (2017b). Integrated genomic characterization of oesophageal carcinoma. Nature *541*, 169–175.

Crum, C.P., and McKeon, F.D. (2010). p63 in epithelial survival, germ cell surveillance, and neoplasia. Annu. Rev. Pathol. *5*, 349–371.

DeNicola, G.M., Chen, P.H., Mullarky, E., Sudderth, J.A., Hu, Z., Wu, D., Tang, H., Xie, Y., Asara, J.M., Huffman, K.E., et al. (2015). NRF2 regulates serine biosynthesis in non-small cell lung cancer. Nat. Genet. *47*, 1475–1481.

Devineni, D., Polidori, D., Curtin, C.R., Murphy, J., Wang, S.S., Stieltjes, H., and Wajs, E. (2015). Pharmacokinetics and pharmacodynamics of once- and twice-daily multiple-doses of canagliflozin, a selective inhibitor of sodium glucose co-transporter 2, in healthy participants. Int. J. Clin. Pharmacol. Ther. *53*, 438–446.

Dotto, G.P., and Rustgi, A.K. (2016). Squamous Cell Cancers: A Unified Perspective on Biology and Genetics. Cancer Cell *29*, 622–637.

Ferone, G., Song, J.Y., Sutherland, K.D., Bhaskaran, R., Monkhorst, K., Lambooij, J.P., Proost, N., Gargiulo, G., and Berns, A. (2016). SOX2 Is the Determining Oncogenic Switch in Promoting Lung Squamous Cell Carcinoma from Different Cells of Origin. Cancer Cell *30*, 519–532.

Gazdar, A.F., Girard, L., Lockwood, W.W., Lam, W.L., and Minna, J.D. (2010). Lung cancer cell lines as tools for biomedical discovery and research. J. Natl. Cancer Inst. *102*, 1310–1321.

Gentric, G., Mieulet, V., and Mechta-Grigoriou, F. (2017). Heterogeneity in Cancer Metabolism: New Concepts in an Old Field. Antioxid. Redox Signal. *26*, 462–485.

Goodwin, J., Neugent, M.L., Lee, S.Y., Choe, J.H., Choi, H., Jenkins, D.M.R., Ruthenborg, R.J., Robinson, M.W., Jeong, J.Y., Wake, M., et al. (2017). The distinct metabolic phenotype of lung squamous cell carcinoma defines selective vulnerability to glycolytic inhibition. Nat. Commun. *8*, 15503.

Gubbay, J., Collignon, J., Koopman, P., Capel, B., Economou, A., Münsterberg, A., Vivian, N., Goodfellow, P., and Lovell-Badge, R. (1990). A gene mapping to the sex-determining region of the mouse Y chromosome is a member of a novel family of embryonically expressed genes. Nature *346*, 245–250.

Hawley, S.A., Ford, R.J., Smith, B.K., Gowans, G.J., Mancini, S.J., Pitt, R.D., Day, E.A., Salt, I.P., Steinberg, G.R., and Hardie, D.G. (2016). The Na+/Glucose Cotransporter Inhibitor Canagliflozin Activates AMPK by Inhibiting Mitochondrial Function and Increasing Cellular AMP Levels. Diabetes *65*, 2784–2794.

Heinz, S., Benner, C., Spann, N., Bertolino, E., Lin, Y.C., Laslo, P., Cheng, J.X., Murre, C., Singh, H., and Glass, C.K. (2010). Simple combinations of lineage-determining transcription actors prime cis-regulatory elements required for macrophage and B cell identities. Mol. Cell *38*, 576–589.

Hensley, C.T., Faubert, B., Yuan, Q., Lev-Cohain, N., Jin, E., Kim, J., Jiang, L., Ko, B., Skelton, R., Loudat, L., et al. (2016). Metabolic Heterogeneity in Human Lung Tumors. Cell *164*, 681–694.

Hibi, K., Trink, B., Patturajan, M., Westra, W.H., Caballero, O.L., Hill, D.E., Ratovitski, E.A., Jen, J., and Sidransky, D. (2000). AIS is an oncogene amplified in squamous cell carcinoma. Proc. Natl. Acad. Sci. USA *97*, 5462–5467.

Hopkins, B.D., Pauli, C., Du, X., Wang, D.G., Li, X., Wu, D., Amadiume, S.C., Goncalves, M.D., Hodakoski, C., Lundquist, M.R., et al. (2018). Suppression of insulin feedback enhances the efficacy of PI3K inhibitors. Nature *560*, 499–503.

Jackson, E.L., Willis, N., Mercer, K., Bronson, R.T., Crowley, D., Montoya, R., Jacks, T., and Tuveson, D.A. (2001). Analysis of lung tumor initiation and progression using conditional expression of oncogenic K-ras. Genes Dev. *15*, 3243–3248.

Ji, H., Ramsey, M.R., Hayes, D.N., Fan, C., McNamara, K., Kozlowski, P., Torrice, C., Wu, M.C., Shimamura, T., Perera, S.A., et al. (2007). LKB1 modulates lung cancer differentiation and metastasis. Nature *448*, 807–810.

Kang, H.B., Fan, J., Lin, R., Elf, S., Ji, Q., Zhao, L., Jin, L., Seo, J.H., Shan, C., Arbiser, J.L., et al. (2015). Metabolic Rewiring by Oncogenic BRAF V600E Links Ketogenesis Pathway to BRAF-MEK1 Signaling. Mol. Cell *59*, 345–358.

Kepe, V., Scafoglio, C., Liu, J., Yong, W.H., Bergsneider, M., Huang, S.C., Barrio, J.R., and Wright, E.M. (2018). Positron emission tomography of sodium glucose cotransport activity in high grade astrocytomas. J. Neurooncol. *138*, 557–569.

Keyes, W.M., Pecoraro, M., Aranda, V., Vernersson-Lindahl, E., Li, W., Vogel, H., Guo, X., Garcia, E.L., Michurina, T.V., Enikolopov, G., et al. (2011). ΔNp63α is an oncogene that targets chromatin remodeler Lsh to drive skin stem cell proliferation and tumorigenesis. Cell Stem Cell *8*, 164–176.

Kouwenhoven, E.N., Oti, M., Niehues, H., van Heeringen, S.J., Schalkwijk, J., Stunnenberg, H.G., van Bokhoven, H., and Zhou, H. (2015). Transcription factor p63 bookmarks and regulates dynamic enhancers during epidermal differentiation. EMBO Rep. *16*, 863–878.

Kundaje, A., Meuleman, W., Ernst, J., Bilenky, M., Yen, A., Heravi-Moussavi, A., Kheradpour, P., Zhang, Z., Wang, J., Ziller, M.J., et al.; Roadmap Epigenomics Consortium (2015). Integrative analysis of 111 reference human epigenomes. Nature *518*, 317–330.

Li, C., and Lu, H. (2018). Adenosquamous carcinoma of the lung. OncoTargets Ther. *11*, 4829–4835.

Li, F., Han, X., Li, F., Wang, R., Wang, H., Gao, Y., Wang, X., Fang, Z., Zhang, W., Yao, S., et al. (2015). LKB1 Inactivation Elicits a Redox Imbalance to Modulate Non-small Cell Lung Cancer Plasticity and Therapeutic Response. Cancer Cell *27*, 698–711.

Locasale, J.W., and Cantley, L.C. (2011). Metabolic flux and the regulation of mammalian cell growth. Cell Metab. *14*, 443–451.

Luengo, A., Gui, D.Y., and Vander Heiden, M.G. (2017). Targeting Metabolism for Cancer Therapy. Cell Chem. Biol. *24*, 1161–1180.

Melkonian, S.C., Daniel, C.R., Ye, Y., Pierzynski, J.A., Roth, J.A., and Wu, X. (2016). Glycemic Index, Glycemic Load, and Lung Cancer Risk in Non-Hispanic Whites. Cancer Epidemiol. Biomarkers Prev. *25*, 532–539.

Mitsuishi, Y., Taguchi, K., Kawatani, Y., Shibata, T., Nukiwa, T., Aburatani, H., Yamamoto, M., and Motohashi, H. (2012). Nrf2 redirects glucose and glutamine into anabolic pathways in metabolic reprogramming. Cancer Cell *22*, 66–79.

Monzavi-Karbassi, B., Gentry, R., Kaur, V., Siegel, E.R., Jousheghany, F., Medarametla, S., Fuhrman, B.J., Safar, A.M., Hutchins, L.F., and Kieber-Emmons, T. (2016). Pre-diagnosis blood glucose and prognosis in women with breast cancer. Cancer Metab. *4*, 7.

Palm, W., and Thompson, C.B. (2017). Nutrient acquisition strategies of mammalian cells. Nature *546*, 234–242.

Patturajan, M., Nomoto, S., Sommer, M., Fomenkov, A., Hibi, K., Zangen, R., Poliak, N., Califano, J., Trink, B., Ratovitski, E., and Sidransky, D. (2002). DeltaNp63 induces beta-catenin nuclear accumulation and signaling. Cancer Cell *1*, 369–379.

Perez, C.A., Ott, J., Mays, D.J., and Pietenpol, J.A. (2007). p63 consensus DNA-binding site: identification, analysis and application into a p63MH algorithm. Oncogene *26*, 7363–7370.

Ramsey, M.R., Wilson, C., Ory, B., Rothenberg, S.M., Faquin, W., Mills, A.A., and Ellisen, L.W. (2013). FGFR2 signaling underlies p63 oncogenic function in squamous cell carcinoma. J. Clin. Invest. *123*, 3525–3538.

Rao, S.S., Huntley, M.H., Durand, N.C., Stamenova, E.K., Bochkov, I.D., Robinson, J.T., Sanborn, A.L., Machol, I., Omer, A.D., Lander, E.S., and Aiden, E.L. (2014). A 3D map of the human genome at kilobase resolution reveals principles of chromatin looping. Cell *159*, 1665–1680.

Rathmell, J.C., Fox, C.J., Plas, D.R., Hammerman, P.S., Cinalli, R.M., and Thompson, C.B. (2003). Akt-directed glucose metabolism can prevent Bax conformation change and promote growth factor-independent survival. Mol. Cell. Biol. *23*, 7315–7328.

Reményi, A., Lins, K., Nissen, L.J., Reinbold, R., Schöler, H.R., and Wilmanns, M. (2003). Crystal structure of a POU/HMG/DNA ternary complex suggests differential assembly of Oct4 and Sox2 on two enhancers. Genes Dev. *17*, 2048–2059.

Rocco, J.W., and Ellisen, L.W. (2006). p63 and p73: life and death in squamous cell carcinoma. Cell Cycle *5*, 936–940.

Rocco, J.W., Leong, C.O., Kuperwasser, N., DeYoung, M.P., and Ellisen, L.W. (2006). p63 mediates survival in squamous cell carcinoma by suppression of p73-dependent apoptosis. Cancer Cell *9*, 45–56.

Safran, M., Kim, W.Y., Kung, A.L., Horner, J.W., DePinho, R.A., and Kaelin, W.G., Jr. (2003). Mouse reporter strain for noninvasive bioluminescent imaging of cells that have undergone Cre-mediated recombination. Mol. Imaging *2*, 297–302.

Saladi, S.V., Ross, K., Karaayvaz, M., Tata, P.R., Mou, H., Rajagopal, J., Ramaswamy, S., and Ellisen, L.W. (2017). ACTL6A Is Co-Amplified with p63 in Squamous Cell Carcinoma to Drive YAP Activation, Regenerative Proliferation, and Poor Prognosis. Cancer Cell *31*, 35–49.

Scafoglio, C., Hirayama, B.A., Kepe, V., Liu, J., Ghezzi, C., Satyamurthy, N., Moatamed, N.A., Huang, J., Koepsell, H., Barrio, J.R., and Wright, E.M. (2015). Functional expression of sodium-glucose transporters in cancer. Proc. Natl. Acad. Sci. USA *112*, E4111–E4119.

Scafoglio, C.R., Villegas, B., Abdelhady, G., Bailey, S.T., Liu, J., Shirali, A.S., Wallace, W.D., Magyar, C.E., Grogan, T.R., Elashoff, D., et al. (2018). Sodium-glucose transporter 2 is a diagnostic and therapeutic target for early-stage lung adenocarcinoma. Sci. Transl. Med. *10*, eaat5933.

Secker, P.F., Beneke, S., Schlichenmaier, N., Delp, J., Gutbier, S., Leist, M., and Dietrich, D.R. (2018). Canagliflozin mediated dual inhibition of mitochondrial glutamate dehydrogenase and complex I: an off-target adverse effect. Cell Death Dis. *9*, 226.

Shukla, S.K., Gebregiworgis, T., Purohit, V., Chaika, N.V., Gunda, V., Radhakrishnan, P., Mehla, K., Pipinos, I.I., Powers, R., Yu, F., and Singh, P.K. (2014). Metabolic reprogramming induced by ketone bodies diminishes pancreatic cancer cachexia. Cancer Metab. *2*, 18.

Sinclair, A.H., Berta, P., Palmer, M.S., Hawkins, J.R., Griffiths, B.L., Smith, M.J., Foster, J.W., Frischauf, A.M., Lovell-Badge, R., and Goodfellow, P.N. (1990). A gene from the human sex-determining region encodes a protein with homology to a conserved DNA-binding motif. Nature *346*, 240–244.

Su, X., Chakravarti, D., and Flores, E.R. (2013). p63 steps into the limelight: crucial roles in the suppression of tumorigenesis and metastasis. Nat. Rev. Cancer *13*, 136–143.

Vander Heiden, M.G., and DeBerardinis, R.J. (2017). Understanding the Intersections between Metabolism and Cancer Biology. Cell *168*, 657–669.

Villani, L.A., Smith, B.K., Marcinko, K., Ford, R.J., Broadfield, L.A., Green, A.E., Houde, V.P., Muti, P., Tsakiridis, T., and Steinberg, G.R. (2016). The diabetes medication Canagliflozin reduces cancer cell proliferation by inhibiting mitochondrial complex-I supported respiration. Mol. Metab. *5*, 1048–1056.

Viticchiè, G., Agostini, M., Lena, A.M., Mancini, M., Zhou, H., Zolla, L., Dinsdale, D., Saintigny, G., Melino, G., and Candi, E. (2015). p63 supports aerobic

respiration through hexokinase II. Proc. Natl. Acad. Sci. USA *112*, 11577–11582.

Wang, G.X., Tu, H.C., Dong, Y., Skanderup, A.J., Wang, Y., Takeda, S., Ganesan, Y.T., Han, S., Liu, H., Hsieh, J.J., and Cheng, E.H. (2017). ΔNp63 Inhibits Oxidative Stress-Induced Cell Death, Including Ferroptosis, and Cooperates with the BCL-2 Family to Promote Clonogenic Survival. Cell Rep. *21*, 2926–2939.

Warburg, O. (1956a). On respiratory impairment in cancer cells. Science *124*, 269–270.

Warburg, O. (1956b). On the origin of cancer cells. Science *123*, 309–314.

Watanabe, H., Ma, Q., Peng, S., Adelmant, G., Swain, D., Song, W., Fox, C., Francis, J.M., Pedamallu, C.S., DeLuca, D.S., et al. (2014). SOX2 and p63 colocalize at genetic loci in squamous cell carcinomas. J. Clin. Invest. *124*, 1636–1645.

Wright, E.M., Hirayama, B.A., and Loo, D.F. (2007). Active sugar transport in health and disease. J. Intern. Med. *261*, 32–43.

Yamamoto, H., Shigematsu, H., Nomura, M., Lockwood, W.W., Sato, M., Okumura, N., Soh, J., Suzuki, M., Wistuba, I.I., Fong, K.M., et al. (2008). PIK3CA mutations and copy number gains in human lung cancers. Cancer Res. *68*, 6913–6921.

Yan, W., Wistuba, I.I., Emmert-Buck, M.R., and Erickson, H.S. (2011). Squamous Cell Carcinoma - Similarities and Differences among Anatomical Sites. Am. J. Cancer Res. *1*, 275–300.

Yang, A., Kaghad, M., Wang, Y., Gillett, E., Fleming, M.D., Dötsch, V., Andrews, N.C., Caput, D., and McKeon, F. (1998). p63, a p53 homolog at 3q27-29, encodes multiple products with transactivating, death-inducing, and dominant-negative activities. Mol. Cell *2*, 305–316.

Young, C.D., Lewis, A.S., Rudolph, M.C., Ruehle, M.D., Jackman, M.R., Yun, U.J., Ilkun, O., Pereira, R., Abel, E.D., and Anderson, S.M. (2011). Modulation of glucose transporter 1 (GLUT1) expression levels alters mouse mammary tumor cell growth in vitro and in vivo. PLoS One *6*, e23205.

Yun, J., Mullarky, E., Lu, C., Bosch, K.N., Kavalier, A., Rivera, K., Roper, J., Chio, I.I., Giannopoulou, E.G., Rago, C., et al. (2015). Vitamin C selectively kills KRAS and BRAF mutant colorectal cancer cells by targeting GAPDH. Science *350*, 1391–1396.

Zhang, X., Choi, P.S., Francis, J.M., Imielinski, M., Watanabe, H., Cherniack, A.D., and Meyerson, M. (2016). Identification of focally amplified lineage-specific super-enhancers in human epithelial cancers. Nat. Genet. *48*, 176–182.

Ziemer, D.C., Kolm, P., Foster, J.K., Weintraub, W.S., Vaccarino, V., Rhee, M.K., Varughese, R.M., Tsui, C.W., Koch, D.D., Twombly, J.G., et al. (2008). Random plasma glucose in serendipitous screening for glucose intolerance: screening for impaired glucose tolerance study 2. J. Gen. Intern. Med. *23*, 528–535.

STAR★METHODS

KEY RESOURCES TABLE

REAGENT or RESOURCE	SOURCE	IDENTIFIER
Antibodies		
Mouse monoclonal anti-p63	Biocare Medical	Cat# CM163A; Clone 4A4; RRID: AB_10582730
Goat polyclonal anti-p63/TP73L	R&D Systems	Cat# AF1916; RRID: AB_2207174
Rabbit polyclonal anti-p63	Active Motif	Cat# 39739
Rabbit polyclonal anti-Glut-1	Alpha Diagnostic International	Cat# GT11-A; RRID: AB_2190596
Rabbit monoclonal anti-Sox2	Cell Signaling Technology	Cat# 3579; Clone D6D9; RRID: AB_2195767
Rabbit monoclonal anti-Sox2 ChIP Formulated	Cell Signaling Technology	Cat# 5024; Clone D6D9; RRID: AB_1904142
Rabbit monoclonal anti-V5-Tag	Cell Signaling Technology	Cat# 13202; Clone D3H8Q; RRID: AB_2687461
Rabbit polyclonal anti-SGLT2	Abcam	Cat# ab85626; RRID: AB_10674183
Mouse monoclonal anti-β-actin	Sigma-Aldrich	Cat# A5441; Clone AC-15; RRID: AB_476744
Rabbit polyclonal anti-Phospho-INSR(Tyr1361)	ThermoFisher Scientific	Cat# PA5 38283; RRID: AB_2554884
Mouse monoclonal anti-INSR	ThermoFisher Scientific	Cat# AHR0271; Clone CT-3; RRID: AB_2536351
Rabbit monoclonal anti-Phospho-AKT(Ser473)	Cell Signaling Technology	Cat# 4058; Clone 193H12; RRID: AB_331168
Rabbit polyclonal anti-AKT	Cell Signaling Technology	Cat# 9272; RRID: AB_329827
Rabbit monoclonal anti-Phospho-S6(Ser235/236)	Cell Signaling Technology	Cat# 4858; Clone D57.2.2E; RRID: AB_916156
Rabbit monoclonal anti-S6 Ribosomal Protein	Cell Signaling Technology	Cat# 2217; Clone 5G10; RRID: AB_331355
Rabbit monoclonal anti-Phospho-4E-BP1(Thr37/46)	Cell Signaling Technology	Cat# 2855; Clone 236B4; RRID: AB_560835
Rabbit monoclonal anti-4E-BP1	Cell Signaling Technology	Cat# 9644; Clone 53H11; RRID: AB_2097841
Mouse monoclonal anti-TTF-1	Dako	Cat# M3575; Clone 8G7G3/7; RRID: AB_531460
Rabbit monoclonal anti-Ki67	Cell Signaling Technology	Cat# 12202; Clone D3B5; RRID: AB_2620142
Rabbit monoclonal anti-CC3(Asp175)	Cell Signaling Technology	Cat# 9664; Clone 5A1E; RRID: AB_2070042
Rabbit polyclonal anti-4-Hydroxynonenal	Abcam	Cat# ab46545; RRID: AB_722490
Rabbit monoclonal anti-Phospho-H2A.X(Ser139)	Cell Signaling Technology	Cat# 9718; Clone 20E3; RRID: AB_2118009
Rabbit monoclonal anti-CK5	Abcam	Cat# ab52635; Clone EP1601Y; RRID: AB_869890
Rabbit monoclonal anti-Acetly-Histone-H3(Lys27)	Cell Signaling Technology	Cat# 8173; Clone D5E4; RRID: AB_10949503
Mouse monoclonal anti-PCNA	Cell Signaling Technology	Cat# 2586; Clone PC10; RRID: AB_2160343
Bacterial and Virus Strains		
Adenoviral Cre (Ad5-CMV-Cre)	Baylor Vector Development Laboratory	N/A

(*Continued on next page*)

Continued

REAGENT or RESOURCE	SOURCE	IDENTIFIER
Biological Samples		
Human lung cancer IHC slides	National Biobank of Korea-Kyungpook National University Hospital	N/A
Human esophageal cancer IHC slides	National Biobank of Korea-Kyungpook National University Hospital	N/A
Human cervical cancer IHC slides	National Biobank of Korea-Kyungpook National University Hospital	N/A
Human head and neck cancer IHC slides	National Biobank of Korea-Kyungpook National University Hospital	N/A
Human skin cancer IHC slides	National Biobank of Korea-Kyungpook National University Hospital	N/A
Human lung cancer tissue microarrays	National Biobank of Korea-Kyungpook National University Hospital	N/A
Human lung cancer tissue microarrays	US Biomax	Cat# LC806, LC2085a, LC2081
Human esophageal cancer tissue microarrays	US Biomax	Cat# ES2081
Human cervical cancer tissue microarrays	US Biomax	Cat# CR2089
Human head and neck cancer tissue microarrays	US Biomax	Cat# OR802
Human skin cancer tissue microarrays	US Biomax	Cat# SK2081
Chemicals, Peptides, and Recombinant Proteins		
WZB117	Calbiochem	Cat# 400036
2-DG	Santa Cruz Biotechnology	Cat# 154-17-6
N-acetyl-cysteine	Sigma-Aldrich	Cat# A9165
[U-13C] Glucose	Cambridge Isotope Labs	Cat# CLM-1396
Insulin	Sigma-Aldrich	Cat# I1884
Matrigel basement membrane	Corning Life Sciences	Cat# 354234
Cisplatin	Sigma-Aldrich	Cat# P4394
Luciferin	PerkinElmer	Cat# 122799
Canagliflozin	SelleckChem	Cat# S2760
Critical Commercial Assays		
NADP/NADPH-Glo assay kit	Promega	Cat# G9081
GSH/GSSG-Glo assay kit	Promega	Cat# V6611
Glucose uptake cell-based kit	Cayman	Cat# 600470
DHE assay kit	Cayman	Cat# 601290
C11-BOIDPY assay kit	Invitrogen	Cat# D3861
H2DCFDA assay kit	Cayman	Cat# 601520
L-Lactate assay kit	Eton	Cat# 1200014002
Luciferase assay system	Promega	Cat# E4030
Insulin ELISA Kit	Crystal Chem	Cat# 90080
Deposited Data		
p63 ChIP-seq dataset	Saladi et al., 2017	GEO: GSE88859
SOX2 ChIP-seq dataset	Watanabe et al., 2014	GEO: GSE46837
H3K27ac ChIP-seq dataset	Kundaje et al., 2015	GEO: GSM733684
Primary tumors expression data	TCGA	http://www.cbioportal.org
Squamous carcinomas expression data	TCGA	http://www.cbioportal.org
Non-squamous carcinomas expression data	TCGA	http://www.cbioportal.org
Experimental Models: Cell Lines		
HCC2814	Gazdar et al., 2010 (University of Texas Southwestern Medical Center)	N/A
HCC95	Gazdar et al., 2010 (University of Texas Southwestern Medical Center)	N/A

(*Continued on next page*)

Continued

REAGENT or RESOURCE	SOURCE	IDENTIFIER
HCC1588	Gazdar et al., 2010 (University of Texas Southwestern Medical Center)	N/A
A549	Gazdar et al., 2010 (University of Texas Southwestern Medical Center)	N/A
H522	Gazdar et al., 2010 (University of Texas Southwestern Medical Center)	N/A
H1299	Gazdar et al., 2010 (University of Texas Southwestern Medical Center)	N/A
KYSE70	David Wang Lab (University of Texas Southwestern Medical Center)	N/A
KYSE30	David Wang Lab (University of Texas Southwestern Medical Center)	N/A
KYSE510	David Wang Lab (University of Texas Southwestern Medical Center)	N/A
OE33	Wei Zhang Lab (University of Texas Southwestern Medical Center)	N/A
FLO-1	Zui Pan Lab (University of Texas Arlington)	N/A
A431	Richard Wang Lab (University of Texas Southwestern Medical Center)	N/A
A375	Richard Wang Lab (University of Texas Southwestern Medical Center)	N/A
SkMel28	Richard Wang Lab (University of Texas Southwestern Medical Center)	N/A
JHU-029	David Sidransky Lab (Johns Hopkins University)	N/A
OSC19	Vlad Sandulache Lab (Baylor College of Medicine)	N/A
NH31	Ralph Weichselbaum Lab (University of Chicago)	N/A
SCC61	David Wang Lab (University of Texas Southwestern Medical Center)	N/A
Experimental Models: Organisms/Strains		
Mouse strain: NSG; NOD.Cg-Prkdc^{scid}IL2rg^{tm1Wjl}/ Szj	The Jackson Laboratory	Cat# 005557
Mouse strain: NOD/SCID; NOD.CB17-Prkdc^{scid}/J	The Jackson Laboratory	Cat# 001303
Mouse strain: NU/J; FOXN1^{nu}	The Jackson Laboratory	Cat# 002019
Mouse strain: B6.129S4-Kras^{tm4Tyj}/J	The Jackson Laboratory	Cat# 008179
Mouse strain: STOCK Stk11$^{tm1.1Sjm}$/J	The Jackson Laboratory	Cat# 014143
Mouse strain: FVB.129S6(B6)-Gt(ROSA)26Sor$^{tm1(Luc)Kael}$/J	The Jackson Laboratory	Cat# 005125
Mouse strain: FVB; GLUT1$^{flox/flox}$	E. Dale Abel Lab (University of Iowa)	N/A
Oligonucleotides		
Primers for RT-PCR: see Table S1	This paper	N/A
Primers for CHIP-PCR: see Table S1	This paper	N/A
Primers for Cloning: see Table S1	This paper	N/A
shRNA targeting sequence: see Table S2	This paper	N/A
Recombinant DNA		
lenti-CRISPRv2	Addgene	Cat# 52961
pMD2-VSVG	Addgene	Cat# 12259
psPAX2	Addgene	Cat# 12260
pLKO.1-shp63#1	Sigma-Aldrich	Cat# TRCN0000006560
pLKO.1-shp63#2	Sigma-Aldrich	Cat# TRCN0000006502

(*Continued on next page*)

Continued

REAGENT or RESOURCE	SOURCE	IDENTIFIER
pLKO.1-shGLUT1	Sigma-Aldrich	Cat# TRCN0000043583
pLKO.1-shSOX2#1	Sigma-Aldrich	Cat# TRCN0000231643
pLKO.1-shSOX2#2	Sigma-Aldrich	Cat# TRCN0000355637
pLKO.1-puro	Addgene	Cat# 10878
Tet-pLKO.1-puro	Addgene	Cat# 21915
pGL3 vector	Promega	Cat# E1741
pCMV-b-galactosidase	Addgene	Cat# 20702
Software and Algorithms		
IVIS Lumina III Imager	PerkinElmer	Cat# CLS136334
Living Image 4.5V	PerkinElmer	N/A
GC/MS	Shulaev Vladimir Lab (University of North Texas)	N/A
CFX-96 Real-time PCR System	BioRad	Cat# 1855196
Fiji	NIH	N/A
Nikon Eclipse Ni-U microscope	Nikon	N/A
NIS Elements imaging	Nikon	N/A
ChemiDoc	BioRad	Cat# 12003153
Homer Software	Heinz et al., 2010	http://homer.ucsd.edu/homer/ngs/peakMotifs.html
Other		
Normal Chow	Research Diet	Cat# D16062901
Ketogenic Diet	Research Diet	Cat# D16062902
Doxycycline Diet	Research Diet	Cat# D18042704

LEAD CONTACT AND MATERIALS AVAILABILITY

This study did not generate new unique reagents. However, further information, requests for resources and reagents, and questions relating to experimental protocols should be directed to and will be fulfilled by the Lead Contact, Jung-whan Kim (jay.kim@utdallas.edu).

EXPERIMENTAL MODEL AND SUBJECT DETAILS

Human Tumor Samples and Survival Analyses

Human lung SCC (77 and 74 year-old males), head and neck SCC (60 and 48 year-old males and 47 year-old female), esophageal SCC (77 and 51 year-old males), cervical SCC (78 and 58 year-old females), skin CC (64 and 59 year-old males) tumor tissue specimens and patient clinical information were provided by the National Biobank of Korea-Kyungpook National University Hospital (NBK-KNUH). Human lung tumor tissue microarrays established from a cohort of 237 lung cancer patients (161 males and 76 females) with an average age of 65.1 (range 35 – 87) were provided by the NBK-KNUH. Lung (LC806, LC2085a, LC2081), head and neck (OR802), esophageal (ES2081), cervical (CR2089), and skin (SK2081) tumor tissue microarrays were purchased from US Biomax (Derwood, MD, USA), and patient clinical information is available on the website (https://biomax.us). To evaluate if high blood glucose levels in lung SCC patients correlate with overall survival (OS), we analyzed a cohort of 127 non-diabetic lung SCC patients (118 males and 9 females) with an average age of 63.6 (range 42 – 82) and 120 non-diabetic lung ADC patients (64 males and 56 females) with an average age of 60.7 (range 35 – 79) who underwent surgical resection. We also analyzed 65 non-diabetic esophageal SCC patients (56 males and 9 females) with an average age of 65.4 (range 44 – 81) who underwent concurrent chemo-radiation for curative intents. For the blood glucose level, fasting glucose level was not on the list of the routine laboratory tests at the time of cancer diagnosis of each patient. Instead, all the patients were initially tested for random blood glucose (RBG) level, which is a commonly used opportunistic screen for dysglycemia (Ziemer et al., 2008). We adopted RBG $\geq$ 120 mg/dL to be an indication of disorders in glucose metabolism because RBG $\geq$ 120 mg/dL have been shown to have 92% specificity for detection of any glucose intolerance (Monzavi-Karbassi et al., 2016; Ziemer et al., 2008). OS was measured from the day of surgery or start of chemo-radiation until the date of cancer-specific death or to the date of the last follow-up. The survival estimates were calculated using the Kaplan-Meier method and the differences in OS between high and low glucose were compared using the log-rank test. All materials derived from

the NBK-KNUH were obtained from patients under institutional review board-approved protocols. Informed written consent was obtained from all patients, and the study protocol was approved by the institutional review boards of KNUH and University of Texas at Dallas.

Mice

LSL-Kras^{G12D} mice (Jackson et al., 2001), *Lkb1*$^{flox/flox}$ mice (Bardeesy et al., 2002) and *LSL-Luciferase (LSL-Luc)* mice (Safran et al., 2003) were purchased from the Jackson Laboratory (Bar Harbor, ME, USA) and backcrossed more than fifteen generations into the FVB/N inbred mouse strain. *Glut1*$^{flox/flox}$ mice were described previously (Young et al., 2011). All mice were maintained in the pathogen-free Animal Resource Center at the University of Texas at Dallas. Both male and female mice were used. All animal experiments were conducted using age and gender-matched littermate controls. All care and experimental procedures involving mice were approved by the University of Texas at Dallas Institutional Animal Care and Use Committee.

Cell Line

Lung SCC lines HCC2814, HCC95, HCC1588 and lung ADC lines A549, H522, H1299 were obtained from the Hamon Cancer Center Collection (University of Texas Southwestern Medical Center) (Gazdar et al., 2010). Esophageal SCC lines KYSE70, KYSE30, KYSE510 and esophageal ADC lines OE33, FLO-1 were provided by Drs. David Wang and Wei Zhang (University of Texas Southwestern Medical Center). Skin SCC line A431 and melanoma lines A375 and SkMel28 were provided by Dr. Richard Wang (University of Texas Southwestern Medical Center). HN SCC line, JHU-029 was provided by Dr. David Sidransky (Johns Hopkins University). HN SCC lines OSC19, NH31, SCC61 were provided by Drs. Vlad Sandulache (Baylor College of Medicine), Ralph Weichselbaum (University of Chicago), and Jeffrey Myers (MD Anderson Cancer Center). Cells were cultured in 10 mM glucose DMEM (Sigma) supplemented with 5% fetal bovine serum (Sigma), 1% penicillin/streptomycin (Sigma) and 1% non-essential amino acids (Sigma) at 37°C in a humidified 5% CO_2 environment. All cell lines were mycoplasma tested with e-Myco Kit (Boca Scientific).

METHOD DETAILS

In Vivo Tumor Xenograft Experiments

5×10^6 cells suspended in 50% matrigel (Corning Life Sciences) and 50% Hank's Balanced Salt Solution (HBSS, Sigma) were subcutaneously implanted into the flank of nu/nu (*Foxn1*^{nu}) mice or NOD/SCID mice (Jackson Laboratory) between 4 and 6 weeks old. Cisplatin (Sigma) was administered intraperitoneally (i.p.) at 3.5 mg kg^{-1} in PBS (Sigma) twice weekly. 2-Deoxyglucose (2-DG, Santa Cruz Biotechnology) 500 mg kg^{-1} or WZB117 (Calbiochem) 10 mg kg^{-1} was administered i.p. once daily. Tumor volume was measured at indicated times using electronic calipers and estimated by the modified ellipsoid formula: tumor volume = (length x width^2) / 2.

In Vivo KL_{Luc} Mice Experiments

Lung cancer was induced by intratracheal injection of adenovirus-Cre (Baylor Vector Development Laboratory) into 8 weeks-old *LSL-Kras*^{G12D}; *Lkb1*$^{flox/flox}$; *LSL-Luc* (*KL*$_{Luc}$) at 5×10^6 PFU per mouse. Lung cancer progression was monitored via bioluminescence imaging. Luciferin (Sigma-Aldrich) was administered at 150 mg/kg through subcutaneous injection in the neck. Bioluminescence imaging was performed via IVIS Lumina III imager (PerkinElmer). Bioluminoscore was quantified via Living Image 4.5V.

Ketogenic Diet and Canagliflozin Treatment

Mice were fed a control, normal chow (Research Diet, D16062901; 55% carbohydrate, 25% fat, and 20% protein), a ketogenic diet (Research Diet, D16062902; 0.1% carbohydrate, 89.9% fat, and 10% protein) or Doxycycline containing diet (625 mg/kg, Research Diet, D18042704) *ad libitum.* The ketogenic diet was prepared as a paste on a ceramic dish and placed upside down in the food hopper. Ketogenic diet was started when xenograft tumors were approximately 100 mm^3 or 5 weeks after intratracheal inhalation of adenovirus-Cre in KL_{Luc} mice and continued until the mice were euthanized for tissue collection. The doxycycline diet was started when xenograft tumors were approximately 200 mm^3. Canagliflozin (SelleckChem) was dissolved in 0.5% hydroxypropyl methylcellulose (Sigma) and administrated 20 mg/kg via oral gavage daily. Canagliflozin was started 5 weeks after intratracheal inhalation of adenovirus-Cre in KL_{Luc} mice and continued until the mice were euthanized for tissue collection.

Blood Glucose and Insulin Measurement

Blood collected from the tail of mice fasted for six hours prior was utilized to measure blood glucose via glucometer (ONETOUCH Ultra2). Up to 200 μL of blood was collected from the tail into EDTA coated microfuge tube and centrifuged to isolate plasma for insulin measurement. Insulin levels were determined via Mouse Insulin ELISA Assay Kit (Crystal Chem) according to the manufacturer's instruction.

Immunoblot Analysis

Cells were lysed by RIPA lysis buffer supplemented with cOmplete Protease Inhibitor (Roche) and subsequent 20% amplitude sonication for 5 s, and lysates were cleared by 14,000 rpm centrifugation at 4°C for 15 min. Equivalent lysates were separated by

SDS-PAGE and electrotransferred onto polyvinylidene difluoride membranes (Fisher Scientific). Membranes following blocking in 5% non-fat dry milk dissolved in TBST for 30 min were incubated in primary antibody diluted in 5% BSA overnight. Horseradish-peroxidase conjugated secondary antibodies diluted 1:5000 in 5% non-fat milk were used and visualized with SuperSignal West Pico or Femto substrate kits (ThermoFisher). The following commercial primary antibodies supplemented with 0.02% sodium azide were used for immunoblot analysis: p63 (1:1,000; Biocare Medical CM163A), GLUT1 (1:1,000; Alpha Diagnostics GT11-A), SOX2 (1:1,000; Cell Signaling Technology #3579), V5-tag (1:1,000; Cell Signaling Technology #13202), SLGT2 (1:1,000; abcam ab85626), Tyr1361-p-INSR (1:1,000; ThermoFisher Scientific PA5-38283), INSR (1:1,000; ThermoFisher Scientifc AHR0271), Ser473-p-AKT (1:1000; Cell Signaling Technology #4058), p-AKT (1:1,000; Cell Signaling Technology #9272), Ser235/236-p-S6 (1:1,000; Cell Signaling Technology #4858), S6 Ribosomal Protein (1:1,000; Cell Signaling Technology #2217), Thr37/46-p-4EBP1 (1:1,000; Cell Signaling Technology #2855), 4E-BP1 (1:1,000; Cell Signaling Technology #9644), PCNA (1:1,000; Cell Signaling Technology #13110), Cleaved Caspase-3 (1:1,000; Cell Signaling Technology #9664), and β-actin (1:5,000; Sigma A5441). Unprocessed immunoblot images are provided in Data S1.

mRNA Quantification

RNA was isolated using the Direct-zol RNA MiniPrep kit (Zymo Research) from cells lysed with TRI reagent (Sigma) according to manufacturer's protocol. For two-step quantitative RT-PCR, cDNA was synthesized from template RNA by mixing with 5X All-In-One RT MasterMix (abm) then combined with PowerUp SYBR Green Master Mix (Thermo Fisher) as per each manufacturer's instruction. Quantitative PCR was performed using the CFX-96 real-time PCR System (BioRad). Primer sequences used are provided in Table S1.

In Vitro Metabolic Analysis

Glucose uptake was measured using the Glucose Uptake Cell-Based Assay Kit (Cayman) according to the manufacturer's protocol. Following incubation with fluorescent glucose analog 2-NBDG in glucose-free DMEM (GIBCO) at 37°C for 1 hour and cell preparation according to the manufacturer's instruction, emission at 535 nm was measured using a fluorescent confocal microscope (Nikon Eclipse Ni-U) and fluorescent intensity quantified in Fiji (NIH). Conditioned media was collected from cells following 48h proliferation in pyruvate-free, 10mM glucose DMEM in order to quantify extracellular lactate normalized to cell count using the L-Lactate Assay Kit I (Eton). Cellular NADPH and NADP+ levels of cells seeded on white 96-well plates in pyruvate-free 10 mM glucose DMEM and lysed in 1% dodecyltrimethylammonium bromide were assayed using the NADP/NADPH-Glo Assay Kit (Promega) according to manufacturer instruction and raw luminescence normalized to cell count measured by the TC-20 automated cell counter (BioRad). GSH/GSSG ratios were measured in cells seeded in pyruvate-free 10mM glucose DMEM using the GSH/GSSG-Glo Assay (Promega) as specified by manufacturer protocol and normalized to cell count.

In vitro ROS Measurement

ROS levels were detected via H_2DCFDA (Cayman), DHE (Cayman), and C11-BODIPY (Invitrogen). Following seeding on 24-well plates in pyruvate-free, 10 mM glucose DMEM, cells were stained with H_2DCFDA for 1 hour. H_2O_2-treated cells were used as positive control. For ROS measurement by DHE staining, cells were seeded on black 96-well plates in pyruvate-free, 10 mM glucose DMEM, and stained with DHE for 1 hour, and emission measured at 585 nm according to manufacturer's protocol. TBHP or antimycin A was used as positive controls for ROS generation for each assay, and relative fluorescent intensity as a proxy for ROS was normalized to cell count. For lipid peroxidation analysis, cells were seeded on chamber slide (Thermo Fisher) in pyruvate-free, 10 mM glucose DMEM, and stained with C11-BODIPY for 30 minutes. H_2O_2-treated cells were used as positive control. Reduced and oxidized probes were measured respectively at 590 nm and 535 nm. Up to 6 images were taken for quantification.

U-^{13}C Glucose Tracing and GC-MS Metabolomics

Following 24h culturing in pyruvate-free DMEM containing 10mM [U-^{13}C] glucose (Cambridge Isotope Labs), cells were quenched with cold 80% methanol. Polar metabolites were then extracted in 80% methanol containing 0.3 μg/μL myristic-d27 acid (Sigma) and dried via vacuum centrifugation and lyophilization. Dried polar metabolite extracts were derivatized for GC-MS analysis by methoxyamination using 30μL of methoxyamine HCl dissolved in 20mg/mL pyridine for 60 minutes at 60°C and by silyation with 30μL of MSTFA (Sigma) for 60 minutes at room temperature. Derivatized extracts were analyzed on an Agilent 7890 GC / 5975 MDS with a splitless 1μL injection and 10°C/min ramp rate from 70°C – 320°C. Electron impact ionization was utilized for mass spectrum collection, and peak identification and deconvolution were performed using the Agilent ChemStation software with an in-house mass spectrum library. Peaks were integrated and normalized to the myristic-d27 acid standard and further normalized to protein concentration.

Immunoprecipitation (IP)

Following cell lysis with CST lysis buffer (Cell Signaling Technology) supplemented with cOmplete Protease Inhibitor Cocktail (Roche), lysates were cleared by centrifugation at 12,000xg for 15 minutes at 4°C. Dynabeads Protein G (ThermoFisher) were blocked with BSA and incubated with 10 μL of 1 mg/mL antibody overnight at 4°C. Equivalent amounts of cleared cell lysate (200 μg) were then subjected to immunoprecipitation with antibody bound to protein G beads, lysate removed using magnet, and target proteins eluted by adding protein sample buffer and incubating at 90°C for 5 minutes. Immunoblotting was then performed as indicated above. The following antibodies were used: p63 (1 μg/μL; Active Motif #39739), SOX2 (1:100; Cell Signaling Technology #5024).

Chromatin Immunoprecipitation (ChIP)

Cells were cross-linked with 1% formaldehyde (16% methanol free formaldehyde solution (w/v), Thermo Fisher Scientific) in culture medium for 10 min at room temperature with rocking and quenched for 5 min with 1/20 volume of a 2.5 M glycine solution. The cells were washed twice with PBS and harvested by centrifugation at 2,000 g for 10 min at 4°C. The cell pellets were snap frozen in liquid nitrogen and stored at −80°C until use. The frozen cell pellets were resuspended in lysis buffer 1 (0.05 M HEPES pH7.5, 140 mM NaCl, 1 mM EDTA, 10% glycerol, 0.5% NP-40, 0.25% Triton 100, and protease inhibitors) for 10 min at 4°C with rocking. After centrifugation, the cell pellets were resuspended in lysis buffer 2 (10 mM Tris pH 8, 200 mM NaCl, 1 mM EDTA, 0.5 mM EGTA, and protease inhibitors) at room temperature for 10 min with rocking. After pelleting nuclei by centrifugation, chromatin was sheared by Covaris Sonicator (s220) with the following condition; 10%–20% dury cycle, 175-peak intensity power, 200 cycles per burst, 500 s. The chromatin solution was the spun for 10 min at 10,000 g to remove cell debris and stored at −80°C until use. To immunoprecipitated chromatin, Dynabeads Protein G (Thermo Fisher Scientific) was blocked with BSA and incubated overnight with the primary antibody: p63 (1 μg/μL; Active Motif #39739), SOX2 (1:100; Cell Signaling Technology #5024), Acetyl-Histone H3-Lys27 (D5E4, 1:100; Cell Signaling Technology #8173). Pre-coupled Dynabeads were resuspended in ChIP buffer (1% Triton X-100, 100mM NaCl, 0.1% sodium deoxycholate, 0.5% N-lauroylsarcosine, and 0.5 mM EGTA) and mixed with 250 – 500 μg of soluble chromatin. The mixture was incubated at 4°C overnight with rotating, followed by washing with RIPA buffer (50 mM HEPES pH 7.5, 500 mM LiCl, 1 mM EDTA, 1% NP-40, and 0.7% sodium deoxycholate) for a total of eight times. ChIP DNA was eluted from the beads by incubating with 50 μL elution butter (TE with 1% SDS) at 65°C for 15 min with constant agitation, then centrifuged for 1 min at 10,000 g. Supernatant (up to 50 μl) was taken out and mixed with 120 μL of elution buffer and incubated at 65°C overnight to reverse the crosslinks. Protein was removed by incubation with 120 μL of proteinase K solution (2% glycogen, 5% proteinase K solution, 20 mg/ml in TE buffer for 2 hours at 37°C. The sample was then extracted with phenol and chloroform and precipitated with 100% EtOH. The DNA was then treated with 30 μL of TE buffer containing 10 μg of DNase-free RNase A (Sigma, 6513) followed by PCR cleanup to purify DNA. Quantitative real-time PCR was undertaken as described previously. The following antibodies were used. Primer sequences are provided in Table S1.

CRISPR-Cas9 Genome Editing

To generate lentiviral vectors, sgRNAs were created by annealing complementary oligonucleotides with the forward oligonucleotide designed as 5′-CACCG-(20 nt sgRNA target sequence)-3′ and the second oligonucleotide designed as 5′-AAAC-(20 nt reverse complement of the sgRNA target sequence)-C-3′. The sgRNA used to target the p63-binding site in E2 was made by annealing forward primer 5′-caccgCGTGATCAGACTTGCATTGT-3′ and reverse primer 5′-aaacACAATGCAAGTCTGATCACGc-3′. For annealing the oligo pairs, 2 μL of each of the reconstituted oligo solutions (100nM) was mixed with 2 μL of 10X T4 DNA Ligase Buffer (New England Biolabs) and 16 μL dH_2O. The mixtures were heated at 95°C for 4 minutes, then left at room temperature for 60 minutes. The annealed oligos were then diluted 1:200. Next, 1 μg of the lentiCRISPRv2 plasmid (Addgene) was digested with 1 μL Esp3I (Thermo Fisher Scientific) at 37°C for 1 hour and run out on an 1% agarose gel. The 12 kb band was extracted using the QIAquick Gel Extraction Kit (QIAGEN). 1 μL of the oligo mixture was ligated with Esp3I-digested lentiCRISPRv2 using T4 DNA Ligase. 2.5 μL of the resulting ligation mixture was transformed into XL10-Gold Ultracompetent cells (Agilent). Individual colonies were picked, plasmid DNA isolated and sgRNA regions were sequenced with primer 5′-GGGCCTATTTCCCATGATTCCTTCA-3′. To generate the lentiviral particles, HEK293T cells were grown to 50%–70% confluence and then transfected with 3.3 μg of the lentiCRISPRv2 plasmid with the p63-binding site in E2 targeting sgRNA, 3.3 μg of the pMD2-VSVG plasmid, and 3.3 μg of the psPAX2 plasmid using 20 mL of JetPRIME (Polyplus). 24 h later, the medium was removed and replenished with 5 mL of complete growth medium. In the next 3 days, the growth medium containing lentiviral vectors was harvested, and 5 mL of fresh complete growth medium was replenished. The final pooled 15 mL growth medium was centrifuged at 3,000 rpm for 15 min at 4°C to remove cell debris. The supernatant was filtered through a 0.45 μm filter, dispensed into 1–2 mL aliquots and stored at −80°C. Viral titers were determined using qPCR Lentivirus Titration Kit (ABMGood) following manufacturer's instructions. 2.5 million KYSE70 cells were seeded onto a 10 cm Petri dish. 24 hours later, cells were transduced using the lentiviral vectors at a multiplicity of infection (MOI) of 1.0. 48 hours post-transduction, cells were treated with 1.0 μg/mL of puromycin. Polyclonal stable cell line libraries were established after ~2 weeks of drug selection. The p63-binding site in E2 disruption site was sequenced by extracting genomic DNA, amplifying the target region with forward primer 5′-CTGC TCCTTCTTCAAACCACACATCACC-3′ and reverse primer 5′-GACAGAAAGCCTGGCATTCAGTAAAGCG-3′, and sequenced with the primer 5′- GTTTAGTGTGTCACTAGAGTGAACA-3′.

shRNA Knockdown

The following pLKO.1 shRNA were used: shp63 #1 (Mission TRC shRNA, TRCN0000006560, Sigma), shp63 #2 (Mission TRC shRNA, TRCN0000006502, Sigma), shGLUT1 (Mission TRC shRNA, TRCN0000043583, Sigma), shSOX2 #1 (Mission TRC shRNA, TRCN0000231643, Sigma), shSOX2 #2 (Mission TRC shRNA, TRCN0000355637, Sigma). To construct Tet-pLKO.1-shΔNp63, pLKO.1-shΔNp63 #1, pLKO.1-shΔNp63 #2, and pLKO.1-shTAp63, targeting oligonucleotides (Eurofins Genomics) were annealed and cloned into the pLKO.1-puro lentiviral backbone (Addgene #10878) or Tet-pLKO-puro (Addgene #21915) as described in the protocol on the Addgene website. For lentivirus production, HEK293T cells were transfected with viral packaging plasmids psPAX2

(Addgene #12260) and pMD2.G (Addgene #12259), and pLKO.1 shRNA using Lipofectamine 3000 (Invitrogen). Cells were incubated with viral supernatant containing polybrene (8 μg/mL). pLKO.1-shScr was used as a control vector. Targeting sequences for all shRNAs are provided in Table S1.

Luciferase Assays

To construct the *SLC2A1* enhancer luciferase reporter vectors, genomic fragments containing E1, E2 or E3 were PCR amplified using the following primers: E1, 5′-GTAGGCTAGCGAGATTCTAGAATTCTGCCACCCT-3′ (forward) and 5′-GTAGCTCGA-GGCTGGT TCCTGGGCCTCC-3′ (reverse); E2, 5′-GTAGGCTAGCCTGTGTCACCCCA-CGCCTC-3′ (forward) and 5′-GTAGCTCGAGTTTTCCA GAAACAGAACAGGGT-3′ (reverse); E3, 5′GTAGGCTAGCCAGCAGAAACATCACAGTGCC-3′ (forward) and 5′-GTAGCTCGAGTTC TAGTCCTCTCTCCCT-3′ (reverse). Amplified inserts were ligated into the pGL3 vector (Promega), and cloned reporter plasmids were verified by restriction digestion as well as DNA sequencing (Eurofins Genomics). Cells were co-transfected with a mixture containing pGL3-E1, E2, or E3 and pCMV-β-galactosidase (Addgene #20702) using Lipofectamine 3000 (Invitrogen). Luciferase and β-galactosidase activities were measured using a luciferase assay kit (Promega) and a β-gal assay kit (Promega) following the manufacturer's instructions.

Stable Cell Lines

The pLV lentiviral vectors expressing GLUT1, ΔNp63α, Tap63α were constructed using VectorBuilder. To construct stable cell lines, cells were incubated with viral supernatant containing polybrene (8 μg/mL), and the transduced cells were selected with 6 μg/ml blasticidin (Invitrogen) or 2 μg/ml puromycin (Thermo Fisher Scientific) for at least 2 weeks. For monoclonal selection, 1,000 cells were seeded on 150 mm dish with relative puromycin or blasticidin containing media. Up to 10 colonies were picked via cloning cylinder (Corning) and plated in 12-well plate for further amplification.

Immunocytochemistry

Cells seeded on coverslips and allowed to adhere overnight were fixed in 4% paraformaldehyde and permeabilized with 0.5% Triton X-100. Primary antibodies diluted in 3% BSA were applied overnight at 4°C, and fluorophore-conjugated secondary antibodies were then applied to visualize primary antibody staining. Fixed cells were counterstained with 4,6-diamidino-2-phenylindole (DAPI), mounted with Vectashield Mounting Medium (Vector Labs), and observed under a fluorescent microscope (Nikon Eclipse Ni-U). The following primary antibodies were used: GLUT1 (1:250; Alpha Diagnostic GT11-A), p63 (1:200; Biocare Medical CM163A).

Immunohistochemistry and Immunofluorescence Analysis

KL and xenograft mice were perfused with 10 mM EDTA in PBS followed by 4% PFA. Both lung and xenograft tumors were extracted and fixed in 4% PFA for 12 hours and were followed by paraffin embedding. Tissue blocks were then sectioned (5 um) and subjected to heat-mediated antigen retrieval (citrate buffer, pH 6). Goat serum (Sigma) or donkey serum (Sigma) was used to block for 1 hour, and primary antibodies diluted were applied at 4°C overnight. Vectastain ABC (Vector Labs) with DAB substrate (Vector Labs) was used to optimize staining according to the manufacture's protocol. The following primary antibodies were used: p63 (1:200; Biocare Medical; CM163A), p63 (1:100; R&D Systems AF-1916), GLUT1 (1:250; Alpha Diagnostic GT11-A), SGLT2 (1:1000; Abcam ab85626), TTF1 (1:1,000; Dako M3575), Ki67 (1:500; Cell Signaling Technology #12202), Cleaved Caspase-3 (1:200; Cell Signaling Technology #9664), Ser473-p-AKT (1:500; Cell signaling Technology #4058), Ser235/236-p-S6 (1:200; Cell Signaling Technology #4858) and Thr37/46-p-4EBP1 (1:200; Cell Signaling Technology #2855), Ser139-p-Histone H2A.X (1:1,000; Cell Signaling Technology #9718), 4-Hydroxynonenal (1:500; Abcam ab46545), CK5 (1:200; Abcam ab52635). Images were taken via Nikon Eclipse Ni-U microscope with NIS Elements imaging software (Nikon) and quantified using Fiji (NIH).

Soft Agar Colony Formation Analysis

48 hours post viral transduction, 1,000 cells were suspended in DMEM containing 0.3% noble agar (Fisher Scientific) and 5% fetal bovine serum, and layered on DMEM containing 0.5% noble agar and 10% fetal bovine serum in 6-well plate. 200 μL of DMEM was supplemented every two days to replenish evaporated media. Colonies were stained with crystal violet and photographed at day 21. All experiments were performed in triplicate. Images were taken via ChemiDoc (Bio-Rad) and quantified using Fiji (NIH).

TCGA Analyses

Publically available mRNA-sequencing gene expression data were obtained from The Cancer Genome Atlas (TCGA) through the Broad Institute's FireBrowse data portal for all TCGA primary tumors (n = 9,532), the TCGA SCC cohort (n = 1,372), the TCGA BLCA cohort (n = 408), and the TCGA non-SCC cohort (n = 7,752). TCGA gene expression profiles were pre-processed to determine gene expression in terms of transcripts per million mappable reads using the RSEM software package and were further quartile-normalized for comparability between datasets. Log2-transformed TPM expression values were compared among SCC, BLCA, and non-SCC cohorts with t test and multiple testing adjustments. Pearson parametric and Spearman nonparametric correlation analyses of GLUT1 and SCC marker mRNA expression from TCGA combined SCC cohorts were performed in GraphPad Prism.

QUANTIFICATION AND STATISTICAL ANALYSIS

Statistical analyses were performed using StatPlus, Version v5 (AnalystSoft Inc.) and GraphPad Prism 7.0 (GraphPad Software Inc.). All data are expressed as mean ± s.e.m or median ± the interquartile range unless noted otherwise. Two-tailed Student's t test, one-way ANOVA with multiple comparison post hoc test, Kruskal-Wallis nonparametric ANOVA, Chi-Square test and Mann-Whitney U test were used for hypothesis testing, and p values of 0.05 were considered significant. ****$p < 0.0001$, ***$p < 0.001$, **$p < 0.01$, *$p < 0.05$.

DATA AND CODE AVAILABLITY

All TCGA data used in the study were obtained through the FireBrowse data portal (http://firebrowse.org). All data supporting the findings of this study are available within the article and its supplementary information files and from the lead contact upon request.